Material candidates for thermally robust applications of selective thermophotovoltaic emitters

Minsu Oh, John McElearney, Amanda Lemire, and Thomas E. Vandervelde

Phys. Rev. Materials **6**, 110201 — Published 7 November 2022

DOI: 10.1103/PhysRevMaterials.6.110201

Material candidates for thermally robust applications of selective thermophotovoltaic emitters

Minsu Oh, John Mcelearny, Amanda Lemire, and Thomas E. Vandervelde*

Department of Electrical and Computer Engineering, Tufts University, Medford, MA 02155, USA.

As majority of the input energy in power generation or energy consumption processes goes to waste as heat, thermophotovoltaic (TPV) devices provide opportunities for energy recovery from (waste) heat. In TPV systems, the energy conversion performance is impacted by thermal emitters. Due to the high-temperature nature of TPV operation, a long-term stable TPV system requires emitters that can withstand high temperatures without significant degradation of their emission performance. Refractory metals are commonly used as the emitter material due to their higher melting point and optical properties. This paper reviews physical/chemical properties of refractory metals that may affect the emitter's performance at high temperatures; melting point, crystal structure, lattice constants, standard reduction potential, diffusion coefficient, Young's modulus, thermal expansion coefficient, and refractive index. Biological hazards and prices of metals are also explored. In the context of these properties, selective TPV emitters fabricated with refractory metals in the literature are compared on their thermal stability. Finally, material properties are discussed towards achieving thermally robust TPV emitters.

1. Introduction

Lawrence Livermore National Laboratory in the U.S. reports that more than 65% of the total energy input in power generation or energy consumption processes is lost to heat [1]. This percentage indicates that there are enormous opportunities of energy recovery from (waste) heat if we can convert it into a power [2–7]. Energy recovery from waste heat will not only lead to more power available but also to less fossil fuel to be burnt in power plants [4,8]. Thus, the capability of thermophotovoltaics (TPVs) to convert waste heat into electricity has excited energy research community [9–13]. Fig. 1 describes the energy flow with a TPV system and its key components for operation: thermal emitter and photodiode. In a TPV device, Fig. 1b, the emitter absorbs thermal energy from the heat source via conduction, convection, and/or radiation [14,15] and radiates the energy in the form of photons towards the photodiode based on its emission spectrum [14]. Then, using the photovoltaic effect, the diode generates electricity by absorbing the photons with energies greater than the bandgap [16]. In TPV systems, which typically operate with a source temperature higher than 900K [8], the emitter is physically closest to the heat source. TPV emitters, therefore, must withstand the hot environment to maintain their stable operation at increased temperatures. For this reason, materials with a relatively high melting point are often used to fabricate emitters [17]. In general, metals have larger extinction coefficients, imaginary part of refractive index, and a higher melting point. In subwavelength structures, large extinction coefficients of the material can induce higher emission. The optical properties of subwavelength structures can also be engineered by changing their dimensions. Thus, metal-based subwavelength structures present advantages of higher, engineerable emission. This is useful for various source temperatures since the wavelength at which thermal radiation energy peaks varies as a function of temperature.

This work reviews thermal stability and optical performance of TPV emitters fabricated with refractory metals. The performance degradation of TPV emitters is found to be due mostly to their chemical reaction or/and mechanical deformation. These changes in emitters are due to the emitter material's responses to thermal energy or temperature variation. The material properties responsible are characterized as lattice constant, reduction potential, diffusion coefficient, Young's modulus, or thermal expansion coefficient. These properties in combination with one another can cause emissivity degradation of a TPV emitter. In the first half of this paper, we introduce the physical/chemical material properties above and find metals with a melting point higher than 1700°C, refractory metals. We then collect the material property data of refractory metals available in the literature to compare each metal. Biological concerns, due to the high-temperature operation of TPV devices, and prices of the metals are explored as well. After that, detailed reviews on TPV emitters fabricated with refractory metals are provided. Finally, we discuss the material properties for realizing thermally robust TPV emitters.

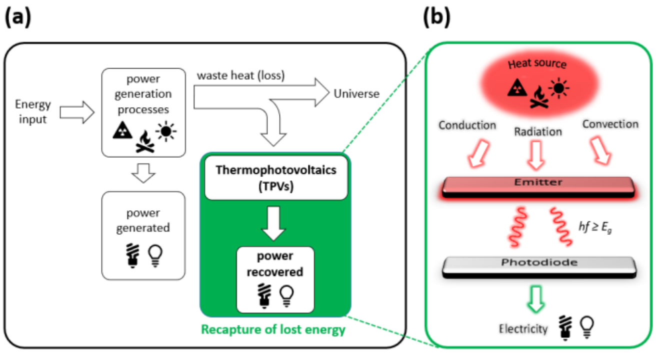

Fig. 1. Thermophotovoltaic (TPV) waste heat recovery. **(a):** Energy flow with TPVs. **(b):** Main components of a TPV system. hf and E_g are photon energy and bandgap energy of the photodiode, respectively.

1.1. Subwavelength structures

Upon interaction between an object and light, every spatial point of the object that the light hits produces its own optical response, also known as the Huygens principle. Thus, the sum of responses from all those points determines the overall optical response of the object. As illustrated in Fig. 2, we compare optical responses of two types of objects: bulk structures and subwavelength structures. For a bulk structure, Fig. 2a, where structure dimensions are much larger than the wavelength, its optical responses can be calculated by relatively simple equations, such as Fresnel coefficients (for reflection and transmission) [18] or absorption coefficient (for absorption) [19]. For a given angle and wavelength of the incident light, the optical responses of a bulk structure are determined by the refractive index and thickness of the material. This, as refractive index is an intrinsic property of a material, fundamentally limits the “engineerability” of the optical interaction of bulk structures. However, as dimensions of a structure decrease close to the wavelength, its optical interactions start to deviate from those it had when it was in a bulk status. Structures where dimensions are smaller than the wavelength are called subwavelength structures, Fig. 2b. Optical responses of subwavelength structures are determined not only by the refractive index and thickness but also by the dimensions, shape, and spatial distribution of the structure elements. Therefore, compared to bulk structures, subwavelength structures allow arbitrary manipulation of their optical responses to a larger degree by changing their geometry as well as constituent materials. For this reason, subwavelength structures, also known as metamaterials (MMs) or photonic crystals (PhCs), are commonly used to create emitters with desired emission spectrum.

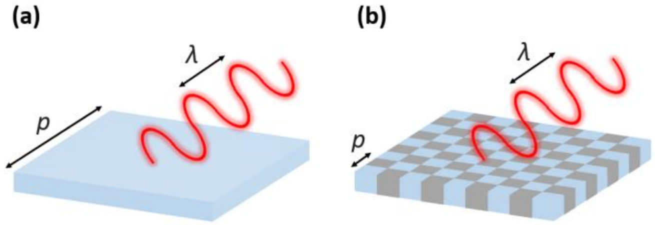

Fig. 2. Comparison of a bulk structure (**a**) and a subwavelength structure (**b**). λ is wavelength of the incident light. Size of p relative to λ distinguishes bulk and subwavelength structures. Objects in blue and gray represent different materials.

1.2. Crystal structure and phase

A crystal (or lattice) structure is a unique pattern of atomic arrangement of the material. Since a crystal structure is determined by how atoms are located with respect to their neighboring atoms, different growth orientations of an atomic stack do not render a different crystal structure. In other words, whether an atomic stack is facing south or north, they are still the same crystal structure. In particular, a region where the atomic arrangement has the same orientation is referred to as a grain. A material may have one or multiple grains while they all have the identical crystal structure. Materials with a single grain are referred to as a single crystal while those with multiple grains are called a polycrystal. Fig. 3 illustrates these crystallographic differences between single crystals and polycrystals of a material with the identical crystal structure. For single crystals, in general, unless the crystal structure allows isotropy, some material properties are dependent on the crystallographic orientation or the direction of measurement [20]. For example, refractive index and thermal expansion coefficient are independent of the orientation in face-centered cubic (FCC) and body-centered cubic (BCC) structures while they vary with the orientation in single crystalline materials with the hexagonal close-packed (HCP) structure [21,22]. Polycrystals, where grains have randomized orientations, however, behave isotropically and exhibit somewhat averaged magnitude of their orientation-dependent properties [20]. Furthermore, thermally excited atoms in neighboring grains in a polycrystal can rearrange, unite, and form a larger grain [23]. This phenomenon, called grain growth, is sometimes used to obtain material properties attributed to larger grains such as lower diffusion coefficient, discussed in detail in Section 1.5, by annealing the material at higher temperatures [24].

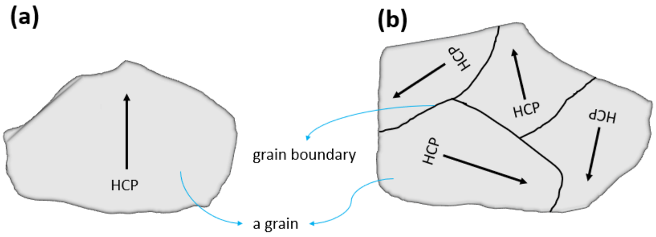

Fig. 3. Grains of a single crystal (**a**) and a polycrystal (**b**). Black arrows in the grains represent the orientation of the atomic stacking within that grain. All grains have the hexagonal close-packed (HCP) structure of atoms.

A homogeneous portion of a material with uniform physical and chemical characteristics is defined as a phase [20]. In practice, a phase of a crystalline solid can be understood as its distinguishing crystal structure [20]. For example, Zr and Hf have the HCP lattice at room temperature, referred to as α-Zr and α-Hf, respectively. As the temperature increases, the lattice structure of these metals changes into the BCC structure (β-Zr and β-Hf) – this phase transition temperature is 863°C and 2115°C for Zr [25] and Hf [26], respectively. Since the atomic arrangement changes upon the phase transition, phase change may cause an abrupt change of the material properties such as lattice constants, volume [27,28], or optical properties [29,30].

1.3. Lattice constant

For a given crystal lattice, we define unit cell as any repeatable shape that can re-create the lattice solely by translation between lattice points: i.e. without rotation or mirroring. It follows that there are multiple possible unit cells for any crystal structure; for example, the cell smallest possible, or with a minimum volume, is defined as primitive cell [31]. By construction, the primitive cell contains only one lattice point. To achieve this, the primitive cell requires lattice points only sit on the vertices of the cell [32]. For some crystal structures, this can obscure important structural information about the lattice in its totality. To better reflect the overall structure and symmetry of the crystal, compared to "primitive cell", "conventional unit cell" is often used instead. The conventional unit cells for the FCC, BCC, and HCP crystal structures are shown in Fig. 4. The dimension of the unit cell in a particular crystallographic direction is then defined as the crystal's lattice constant in that direction: i.e. the distance between adjacent unit cells. For both the FCC and BCC lattice, the lattice constant is equal along all three axes (marked *a* in Fig. 4), while the HCP lattice has different lattice constants between in-plane (marked *a*) and out-of-plane (marked *c*) directions. For this paper, listed lattice constants will refer to those defined by conventional unit cells.

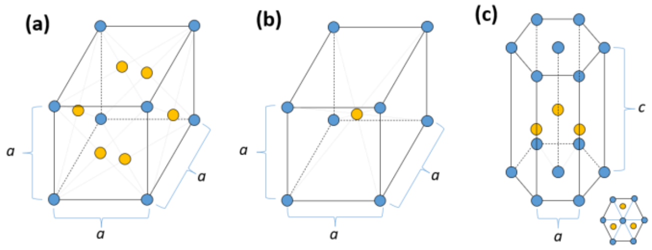

Fig. 4. Conventional unit cells for the FCC (**a**), BCC (**b**), and HCP (**c**) lattices. The coloring of the spheres is meant only to guide the eye – it is not meant to imply different atoms. Given their symmetry, the FCC and BCC lattices are typically given a single lattice constant, marked *a*, which applies along all three Cartesian axes. The HCP is marked with both its in-plane, *a*, and out-of-plane, *c*, lattice constants. The inset in (**c**) is a top view of the HCP unit cell.

It should be noted the lattice constant is typically not equal to the spacing between adjacent atoms. For example, in the FCC lattice, the shortest distance between atoms is the distance between any corner atom and the center atom (labelled A and B in Fig. 5) on one of the adjoining faces. The distance between these two atoms is $\frac{\sqrt{2}a}{2}$, with *a* being the lattice constant. This distinction can become especially important in the case of a crystal with a multi-atom basis. A crystal's basis indicates how many atoms sit on each lattice site. For example, the diamond cubic structure is essentially two interlocking FCC lattices with a single atom on every lattice site. It can alternatively be described as a single FCC lattice with two atoms sitting on each lattice site, separated by a distance of $\frac{a}{4}$ in each direction. Thus, for the case of the two-atom basis, the nearest neighbor distance would be $\frac{\sqrt{3}a}{4}$, from a blue sphere to a purple one, in Fig. 5b. As these both sit on the same lattice site, however, the lattice constant remains simply *a*.

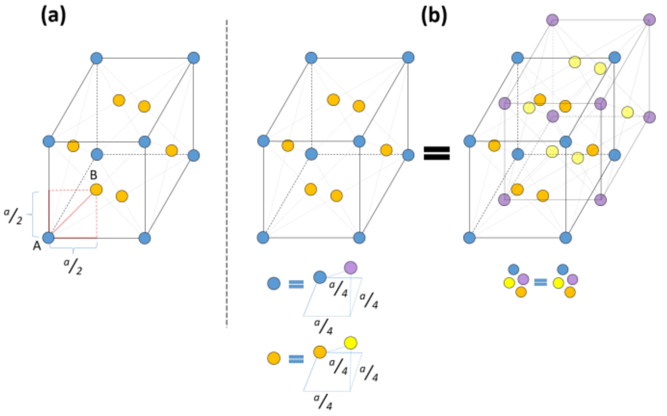

Fig. 5. (**a**): An FCC lattice where the nearest neighbor distance is marked in red. (**b**): The diamond cubic lattice is represented by a single FCC with a two-atom basis (left) and with a single atom basis and the accompanying interlocked FCC lattices (right).

For devices consisted of multiple layers of materials, materials should be chosen to avoid significant lattice mismatch – a difference in lattice constant between adjacent layers – to minimize stress caused by lattice mismatch at the interfaces. Growing layers of significantly different lattice constant, greater than 1% or so, can introduce excessive strain into the crystal [33]. For sufficiently thick layers, this strain can lead to the epilayer delaminating from the underlying stack [34,35]. This effect can also be caused, or exacerbated, by differences in rates of thermal expansion. Two materials with acceptably matched lattice constants at a given temperature can become mismatched, if one is changing at a much higher rate than the other. Thus, an ideal emitter should have well-matched lattice constants between constituent materials at room, growth, and operating temperatures to ensure device integrity. Fig. 6 shows delamination process and some examples of delaminated layers.

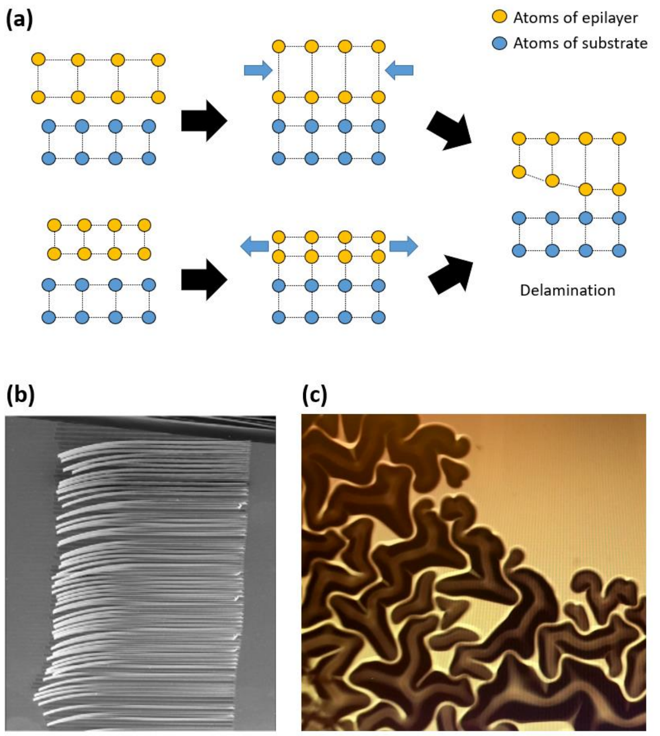

Fig. 6. **(a)**: A schematic view of lattice mismatch-induced strain. Top: an epilayer with lattice constant greater than the underlayer undergoes compressive strain (blue arrows), shrinking the in-plane lattice constant and stretching the out-of-plane. Bottom: an epilayer with lattice constant less than that of the underlayer undergoes tensile strain (blue arrows), stretching the in-plane and shrinking the out-of-plane lattice constants, respectively. **(b)**: Delamination of thin strips of Ni from a Au/Si substrate -reprinted with permission from Ref. [35]. **(c)**: Delamination of a thin Si layer from a quartz substrate.

1.4. Standard reduction potential

The standard reduction potential (SRP) of a chemical species is the magnitude of the electrical potential involved in transferring electrons to the species' cation to reduce it to a neutral state. SRPs are defined with reference to the reduction of protons into H_2: an electrode comprising a Pt crystal submerged in aqueous 1M HCl with H_2 gas bubbled through at 1atm is defined as having a standard potential of zero and is called the standard hydrogen electrode (SHE) [36]. To measure the SRP of a metallic species, the SHE is connected to an electrode of the species across a voltmeter. The electrode being measured is submerged in a solution of a salt containing the species in question; silver, for example, may be measured in a solution of $AgNO_3$. The solutions at each electrode are connected by a salt bridge to maintain charge neutrality. The full system of electrodes and electrolytic solutions is called a galvanic cell. Assembling a galvanic cell produces a spontaneous current flow between the electrodes [37]. The direction of the current flow depends on species under examination: if it is more easily reduced than hydrogen, H_2 gas dissociates at the Pt electrode and electrons flow to the electrode of interest. The species cations combine with the electrons and form a layer of neutral material on the electrode. The voltmeter output while the reaction progresses is the reduction potential, and for a spontaneous reaction in which the species under study is reduced, the SRP is positive. For species which are less easily reduced than H_2, the reaction would proceed spontaneously in reverse: the species electrode oxidizes and sends electrons to the SHE to reduce hydrogen ions to H_2. The recorded SRP would be negative. Therefore, a species with a higher SRP is more resistant to oxidation. As oxidation or reduction is a spontaneous reaction, TPV emitters fabricated with a material with a lower reduction potential, such as W, may suffer optical performance degradation due to oxidation [38–40]. The SRPs, furthermore, are presented as half-reactions, as can be seen in Table 1. The half-reaction for the SHE, for example, is written as $2H^+ + 2e^- \rightleftharpoons H_2$, $E° = 0$ V, where E° is the SRP. In principle, reduction reactions are reversible, with the same potential energy barrier in either direction. Thus, for a given species, its standard oxidation potential is therefore equal in magnitude as its SRP with an opposite sign. Since SRP is an intensive property, the magnitude of the recorded voltage is independent of the size of the electrodes used. While temperature can impact the SRP, its effects are relatively small [41,42].

1.5. Diffusion

Diffusion is a translational movement of a thermally excited atom (or atoms) where the atoms move to other locations. As diffusion is physical movement of atoms through the volume or surface of a material, it is responsible for physical/chemical reactions such as grain growth [43] or oxidation [38]. According to the Maxwell-Boltzmann distribution [44], at thermal equilibrium, a portion of atoms in the system have higher kinetic energy than others. The atoms with higher kinetic energy may have enough energy to break their atomic bonding with neighboring atoms and move to other locations. As thermal energy fuels this kinetic movement, generally, a higher temperature causes more diffusion. The relationship between diffusion and temperature is represented by $D = A(-Q/k_B T)$. D is diffusion coefficient (the higher the value, the more diffusion), A is a temperature-independent constant, Q is activation energy for diffusion, k_B is Boltzmann constant, and T is temperature [20]. As the likelihood of diffusion increases exponentially as a function of temperature, nanostructures can be deformed due to diffusion at high temperatures [45–47]. In particular, the diffusion coefficient of a material is higher in its polycrystalline status than its single crystal since grain boundaries, where the number density of atoms is lower than that within a grain, behave as a tunnel through which atoms can move more easily [48]. For this reason, at high temperatures, the optical performance of nanostructured polycrystalline emitters can degrade more than a single crystalline nanostructure does [49].

1.6. Thermal expansion and Young's modulus

As thermal energy leads to more movements of atoms, the average distance between atoms increases as the temperature increases. This results in expansion of the material dimensions, referred to as thermal expansion. Upon heating, the expansion of a material in length is measured as coefficient of linear thermal expansion, α_L or typically referred to as CTE. The coefficient is defined as $\alpha_L = \frac{1}{L_o}\frac{dL}{dT}$, where L_o is length of the material before temperature change, and dL and dT are variation in length and temperature, respectively. As different materials may have different CTEs, thermal expansion can create stress at interfaces between jointed materials. If the stress is too high, the atomic bonding at the interface may rupture, which can cause the materials to delaminate. This can lead to a permanent fracture and severe optical performance degradation of an emitter fabricated with multiple materials [50]. Moreover, the resistance of a material to one-dimensional tensile or compressive stress is measured as Young's modulus, E_{Young}, defined as applied stress divided by the strain [51]. Thus, at a given strain, materials with a higher Young's modulus is under more stress than those with a lower modulus. This indicates that a higher Young's modulus may contribute to delamination at interfaces upon thermal expansion. Fig. 7 describes delamination due to a higher Young's modulus.

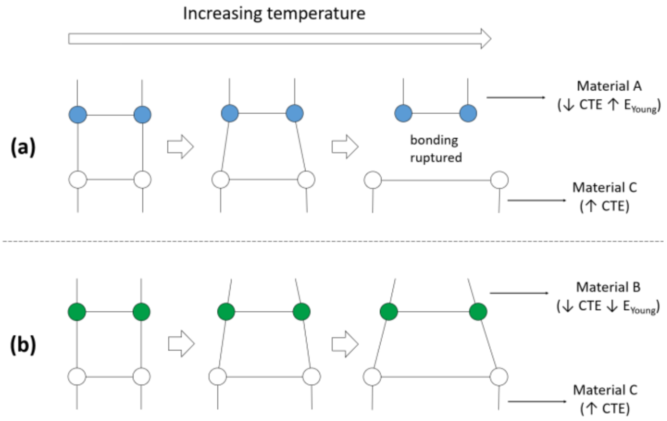

Fig. 7. Delamination due to a higher Young's modulus upon thermal expansion. Materials with a higher (**a**) and lower (**b**) Young's modulus are compared. Atoms and atomic bonding are represented by balls and lines, respectively. The upward (↑) and downward (↓) arrows represent high and low values of the property, respectively.

2. Refractory Metals

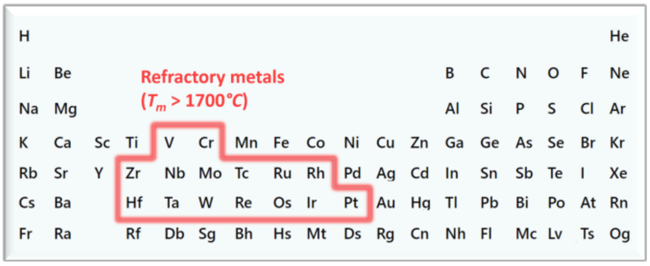

Fig. 8. Periodic table of elements. Metals with a melting point (T_m) higher than 1700°C are boxed in red.

The 15 refractory metals with a melting point (T_m) higher than 1700°C in the periodic table are shown in Fig. 8. The physical and chemical properties of these metals for TPV applications are tabulated in Table 1 with their biological hazard and typical prices. References to some reported emitters fabricated with those metals are provided in the table as well. These emitters are discussed in Section 3 in detail on their key performance. The complex-valued refractive indices ($\tilde{n} = n + ik$) of the metals are plotted in Fig. 10. n and k are real and imaginary parts of refractive index, respectively. For metals with FCC and BCC structures, being single-crystalline or polycrystalline does not affect their refractive index due to the symmetry of their lattice structure [21]

Table 1. Physical and chemical properties of the 15 refractory metals. T_m is melting point. For the crystal structure, FCC, BCC, and HCP stand for face-centered cubic, body-centered cubic, and hexagonal close-packed, respectively. For the standard reduction potentials, efforts were given to show reactions that involve similar oxidation states, mostly IV, of the metals for objective comparison. Self-diffusion refers to diffusion of the atom in the same-element matrix; diffusion of V atoms in a V matrix for example. s.c. and p.c. stand for single crystal and polycrystal, respectively. CTE shown is the coefficient of linear thermal expansion. While some references report material properties at temperatures specified and some do not, indicating room temperature, values in this table are presumably at room temperature unless otherwise specified. For biological hazard, "high" is given if the material is radioactive or reported lethal. Blank cells indicate that there is no reported or little known information to the best of our knowledge.

	T_m (°C) [52]	**Crystal Structure**	**Lattice Constant (Å)**	**Standard Reduction Potential (V)**	**Self-diffusion Coefficient at 1000°C (10^{-15}cm²/s)**	**Young's Modulus (p.c.) (GPa)** [53,54]	**CTE at 25°C (10^{-6}/K)**	**Biological Hazard**	**Price (USD/g)** [52]	**Reported Emitters**
V	1910	BCC	3.02 [55]	-0.242 [52] $V_2O_5 + 10H^+ + 10e^- \rightleftharpoons 2V + 5H_2O$	81.7 (s.c.) [56] 81.5 (p.c.) [57]	128	8.4 [58]	mid [59]	3	[60]
Cr	1907	BCC	2.88 [55]	-0.188 [52] $CrO_2 + 4H^+ + 4e^- \rightleftharpoons Cr + 2H_2O$	0.945 (s.c.) [61]	279	4.9 [58]	mid [59]	1	[62–65]
Zr[*]	1854	HCP (α-Zr) BCC (β-Zr)	a = b = 3.24 c = 5.17 (α-Zr) [66]	-1.473 [42] $ZrO_2 + 4H^+ + 4e^- \rightleftharpoons Zr + 2H_2O$	1.49×10^6 (β-Zr, p.c.) [61]	97	5.7 (α-Zr, p.c.) [58]	mid [59]	4	-
Nb	2477	BCC	3.30 [55]	-0.690 [52] $NbO_2 + 4H^+ + 4e^- \rightleftharpoons Nb + 2H_2O$	0.036 (s.c. or p.c.) [57]	105	7.3 [58]	mid [67]	0.5	[68]
Mo	2622	BCC	3.15 [55]	-0.152 [52] $MoO_2 + 4H^+ + 4e^- \rightleftharpoons Mo + 4H_2O$	1.5×10^{-4} [†](s.c.) [61] 2.4×10^{-4} [†](p.c.) [57]	325	4.8 [58]	mid [59]	0.16	[69–73]
Tc	2157	HCP	a = b = 2.76 c = 4.42 [66]	+0.272 [74] $TcO_2 + 4H^+ + 4e^+ \rightleftharpoons Tc + 2H_2O$	-	376	-	high (radioactive)	100	-
Ru	2333	HCP	a = b = 2.73 c = 4.31 [66]	+0.788 [52] $RuO_2 + 4H^+ + 4e^- \rightleftharpoons Ru + 2H_2O$	-	420	6.4 (p.c.) [58]	-	25	[75]
Rh	1963	FCC	3.80 [55]	+0.758 [52] $Rh^{3+} + 3e^- \rightleftharpoons Rh$	-	275	8.2 [58]	mid [59]	180	-
Hf[*]	2233	HCP (α-Hf) BCC (β-Hf)	a = b = 3.20 c = 5.08 (α-Hf) [66]	-1.591 [42] $HfO_2 + 4H^+ + 4e^- \rightleftharpoons Hf + 2H_2O$	$\parallel c$ 0.56 [†](α-Hf, s.c.) [61] $\perp c$ 1.43 [†](α-Hf, s.c.) [61] 3.09 (α-Hf, p.c.) [57]	139	6.0 (α-Hf, p.c.) [76]	mid [77]	2	-
Ta	3017	BCC	3.31 [55]	-0.752 [42] $Ta_2O_5 + 10H^+ + 10e^- \rightleftharpoons 2Ta + 5H_2O$	8.7×10^{-4} (s.c.) [61] 1.4×10^{-3} [†](p.c.) [61]	186	6.3 [58]	mid [78]	2	[72,79–81]
W	3414	BCC	3.16 [55]	-0.119 [52] $WO_2 + 4H^+ + 4e^- \rightleftharpoons W + 2H_2O$	1.02×10^{-8} [†](s.c.) [61] 1.9×10^{-4} [†](p.c.) [82,83]	411	4.5 [58]	low – mid [59,84]	2.9	[39,46,49,65,70,72,85–100]
Re	3185	HCP	a = b = 2.78 c = 4.50 [66]	+0.251 [74] $ReO_2 + 4H^+ + 4e^- \rightleftharpoons Re + 2H_2O$	-	470	6.2 (p.c.) [58]	-	16	-
Os	3033	HCP	a = b = 2.76 c = 4.36 [66]	+0.687 [74] $OsO_2 + 4H^+ + 4e^- \rightleftharpoons Os + 2H_2O$	-	550	5.1 (p.c.) [58]	low - high[‡] [101]	100	-
Ir	2446	FCC	3.84 [55]	+0.73 [42] $IrO_2 + 4H^+ + 4e^- \rightleftharpoons Ir + 2H_2O$	3.7×10^{-4} [†](s.c.) [57]	528	6.8 [53]	mid [102]	100	[103–105]
Pt	1768	FCC	3.92 [55]	+0.92 [42] $PtO_2 + 4H^+ + 4e^- \rightleftharpoons Pt + 2H_2O$	1235 (p.c.) [61]	190	8.8 [58]	low-mid [25]	15	[106–111]

[*] The crystal structure of Zr and Hf changes from HCP (α-phase), at room temperature, into BCC (β-phase) at 863°C [25] and 2115°C [26], respectively.

[†] The value is extrapolated for 1000°C (1273K) based on the data in the reference.

[‡] When heated, Os oxidizes into the volatile compound OsO_4 (osmium tetroxide). Although Os itself is innocuous, OsO_4 is reported highly toxic and lethal in animal testing [101].

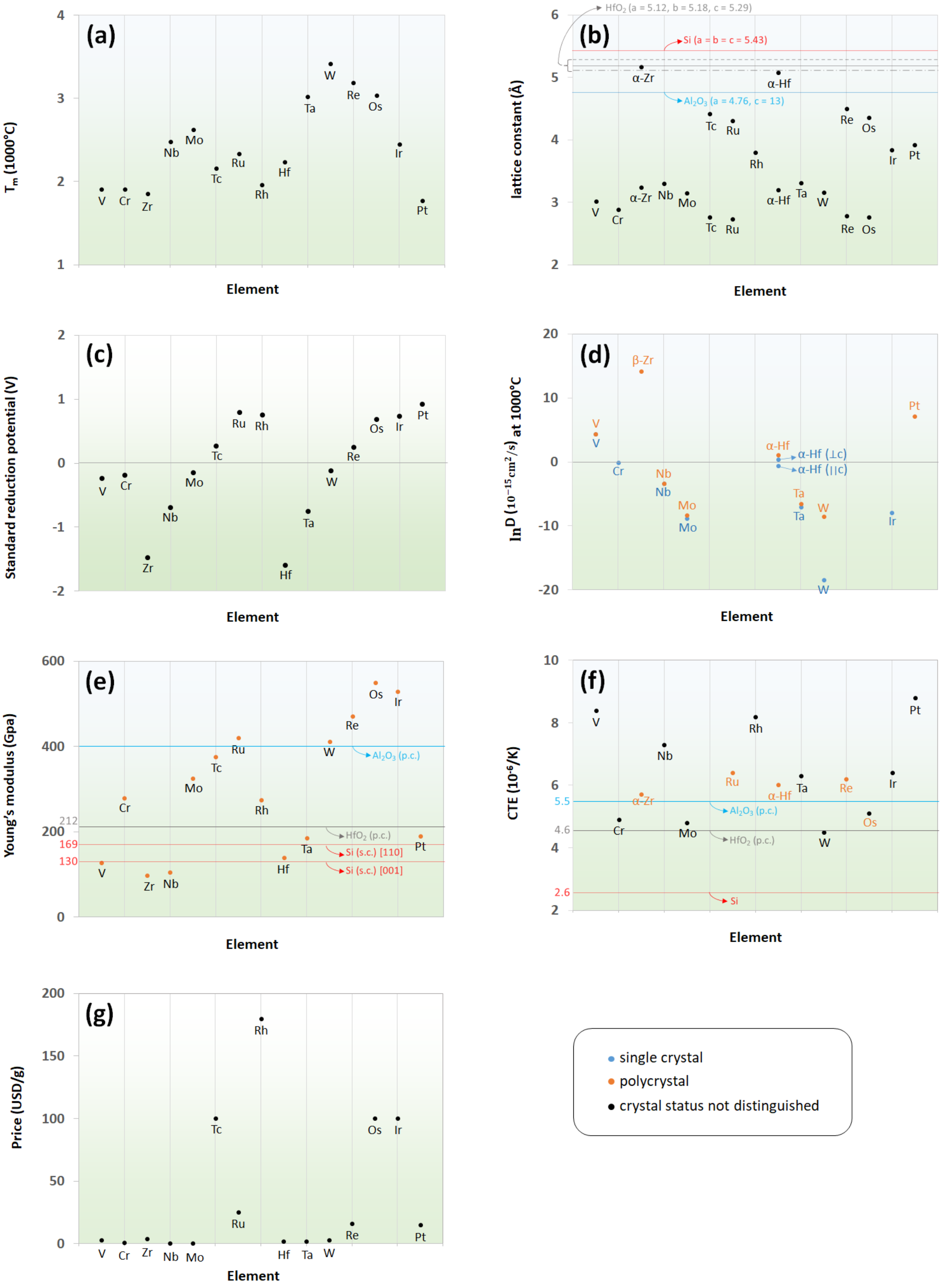

Fig. 9. Properties of the refractory metals from Table 1. Melting point (**a**), lattice constant (**b**), standard reduction potential (**c**), self-diffusion coefficient (D) (**d**), Young's modulus (**e**), linear thermal expansion coefficient (CTE) (**f**), and typical prices (**g**) are shown. Lattice constants are shown along with those of common substrate or coating materials for TPV emitters; Si [55], HfO_2 [112], and Al_2O_3 [113]. Of these materials, Young's moduli [114–116] and CTEs [113,117,118] are shown as well.

FCC and BCC metals (optically isotropic)

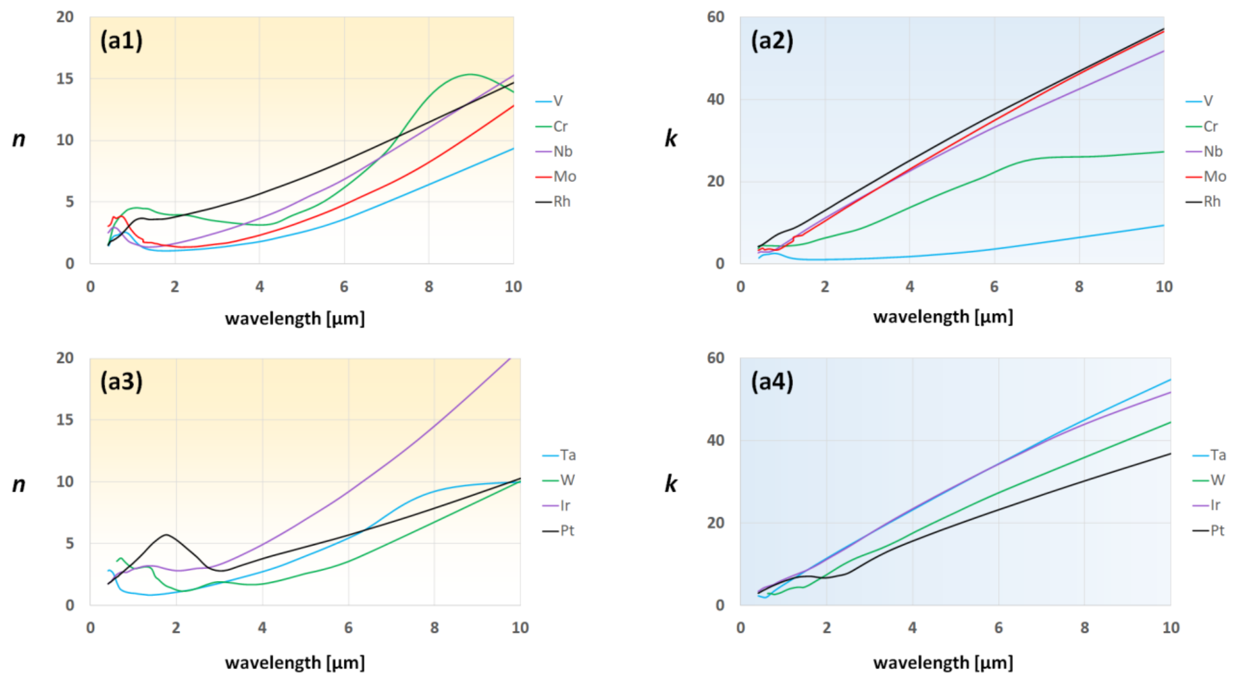

HCP metals (optically anisotropic)

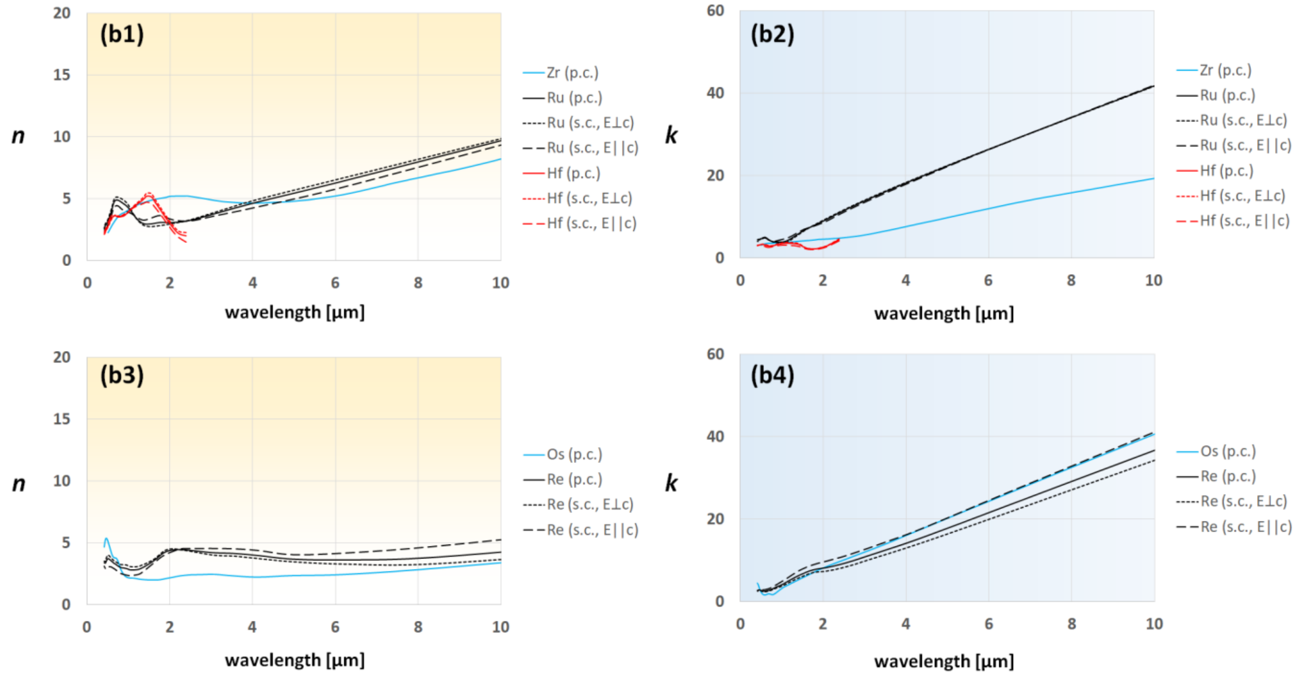

Fig. 10. Refractive index of the refractory metals. Data are separated for optically isotropic (**a**) and anisotropic (**b**) metals. *n* and *k* are real and imaginary parts of refractive index, respectively. In the legend, s.c. and p.c. stand for single crystal and polycrystal, respectively. The orientation of incident electric field (*E*) relative to the orientation of the longer axis of HCP unit cell, c-axis, are notated. Data are from [52,119]. For polycrystalline Ru, Hf, and Re, refractive indices are calculated from the relationships $n + ik = \sqrt{\varepsilon}$ and $\varepsilon = (\varepsilon_{||} + 2\varepsilon_{\perp})/3$, assuming randomized grain orientations [120], where ε is permittivity. We note that $\varepsilon_{||}$ and $\varepsilon_{\perp}$ are permittivities corresponding to electric fields parallel and perpendicular to the c-axis of the HCP unit cell, respectively [120].

3. Selective Emitters Fabricated with Refractory Metals

This section reviews emitters fabricated with refractory metals and their thermal degradation. For thermal degradation, we focus on mechanical deformation or/and changes in emissivity spectrum of emitters since they serve as a more objective measure for comparison. The conversion efficiency and output power of TPV systems are not in focus of this work for the following reasons. No single metric is universally used by researchers to report TPV efficiency. The main difference between different metrics is inclusion [9] or exclusion [121] of the incident power with photon energies smaller than the photodiode's bandgap in the denominator. This means that a TPV system can have different efficiencies depending on which metric is used. Another reason is that there is currently little research on efficiency or output power changes upon the emitter's thermal degradation as most researchers report with the emitter's mechanical deformation or emissivity changes. Nevertheless, degradation in emissivity causes the TPV efficiency and output power to drop [40]. Priority for the review is given to emitters that are reported with experimental results as opposed to simulated results. For metals where there was no emitter reported with experimental results, to the best of our knowledge, emitters demonstrated with simulated results are reviewed. Oftentimes, "emissivity" of emitters are reported based on their "absorptivity" as these two properties have the equal value at a given wavelength, polarization, direction, and temperature due to the Kirchhoff's law [106,122]. For this reason, in this paper, the terms "absorption" and "emission" may be used interchangeably. Moreover, as different literature uses different terms, we note that the terms "absorptivity" or "absorbance" refers to the same quantity in this paper. The same is true for "emissivity" and "emittance" as well as for "reflectance" and "reflectivity".

3.1. Vanadium (V)

A V-based MM thermal emitter is numerically reported by Liu et al. over the visible to infrared wavelengths [60]. By using alternating nano-sized disks of V and SiO_2, the authors of Ref. [60] demonstrate their emitter's radiation spectrum close to that of a blackbody. Fig. 11 shows the structure and simulated spectral radiance curve of the V-based emitter. The radiation properties of this emitter are attributed to plasmonic resonances between the metal disks.

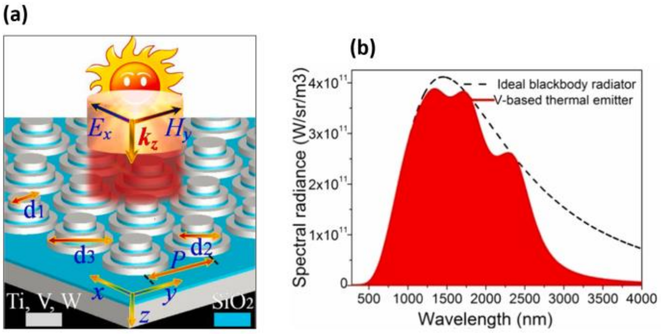

Fig. 11. A V-based emitter. Reprinted with permission from Ref. [60]. **(a):** Emitter structure with three nano-sized disks. White and blue layers are the metal (either all Ti or V or W) and SiO_2, respectively. **(b)**: Simulated spectral radiance curves of the emitter with V disks and a blackbody corresponding to 2000K.

3.2. Chromium (Cr)

Based on optical interference between Cr and SiO_2 layers, Deng et al. experimentally demonstrated a broadband emitter with measured absorption [62]. As the authors of Ref. [62] report, their emitter's emissivity is higher than 90% over the wavelength range 0.4 µm – 1.4 µm. The structure and emission results of this structure are shown in Fig. 12(a). Meanwhile, while focusing on submillimeter wavelengths, a Cr ring resonator is numerically suggested with a potential application as a thermal emitter by Hu et al. [63]. The unit cell and absorption spectrum of this ring resonator are shown in Fig. 12(b). Another emitter fabricated with Cr, where the performance is based on plasmonic resonance, is also reported numerically in the visible – infrared spectrum [64].

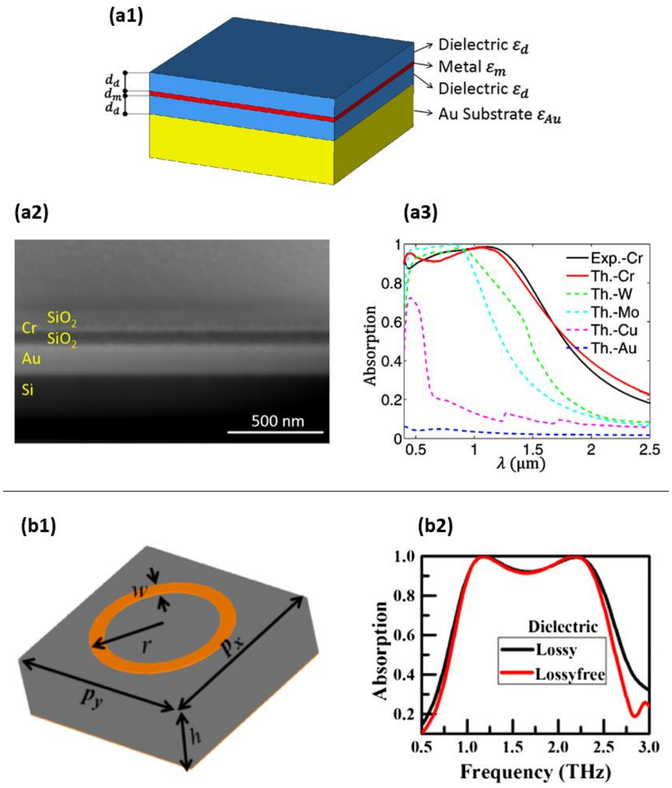

Fig. 12. Cr-based emitters. **(a):** Emitter with Cr (metal) and SiO_2 (dielectric) planar layers [62]. The layer structure (**a1** and **a2**) and measured absorption (Exp.-Cr) (**a3**) are shown. d_d = 85 nm and d_m = 8 nm. **(b):** Emitter with a Cr ring resonator [63]. The unit cell (**b1**) and simulated absorption (**b2**) are shown. Materials in orange and gray are Cr and a dielectric, respectively. w = 4 µm, r = 25 µm, p_x = p_y =70 µm, and h = 26 µm. **(a)** and **(b)** are reprinted with permission from Refs. [62] and [63], respectively. © The Optical Society.

3.3. Niobium (Nb)

While focusing on transmission properties, Nb-based plasmonic MMs with mechanical stability at up to 800°C in vacuum are experimentally demonstrated by Bagheri et al. [68]. They report that the mechanical stability of their structures, in vacuum, can be further improved with a 5 nm-thick Al_2O_3 coating layer on top of the Nb features. The thermal stability improvements are attributed to the prevention of Nb grain growth due to the coating layer. Annealing results of these Al_2O_3-coated MMs are shown in Fig. 13 along with measured transmittance. In the figure, little mechanical deformation of Nb features is seen after annealing. As can be seen in Fig. 13(d), the structures exhibit stable transmission properties before and after annealing. Although these MMs are reported with a focus on their transmission, it is worth noting that these Nb-based MMs maintain stable mechanical and optical properties at elevated temperatures in vacuum. Thus, the results of Ref. [68] may provide insights for creating Nb-based emitters for TPV applications. Additionally, the authors of Ref. [68] state that annealing the structure in air causes oxidation of Nb, which leads to optical performance degradation.

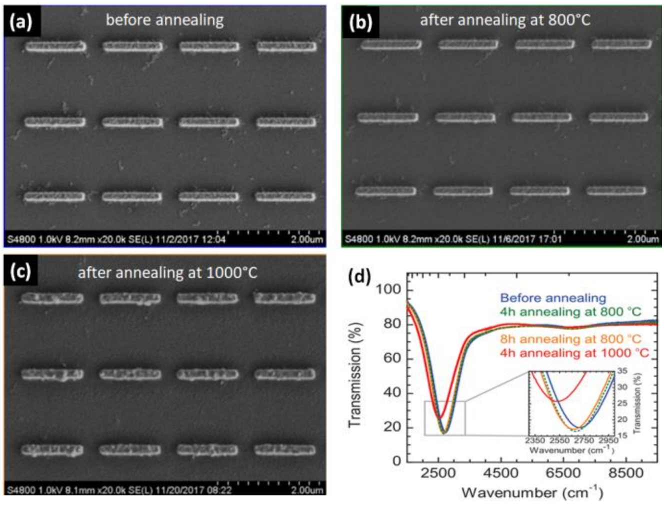

Fig. 13. Nb-based metamaterials with 5 nm-thick Al_2O_3 coating. Reprinted with permission from Ref. [68]. Copyright (2018) American Chemical Society. **(a) – (c):** Scanning electron microscopy (SEM) images of the emitter's top surface before or after annealing in vacuum. **(d):** Measured transmittance of the emitter before and after annealing.

3.4. Molybdenum (Mo)

Thermal emission of a plasmonic MM with Mo disks is experimentally reported by Yokoyama et al. [69]. Fig. 14 shows the MM structure and results of the work. As shown in Fig. 14(b), the structure exhibits stable emission properties up to 1000°C in vacuum over the wavelength range 2 – 14 µm. Moreover, in Fig. 14(c), with slightly different dimensions of the structure, the authors of Ref. [69] further demonstrate its stable reflectance before and after annealing the structure at 1000°C for 3 hours in vacuum. After annealing, as it is stated in Ref. [69], only a small number of Mo disks are deformed while more than 90% of them are undeformed. Scanning electron microscopy (SEM) images of the emitter's surface after annealing are shown in Fig. 14(d) and 14(e). Another nanostructured emitter with Mo coating on a silica woodpile scaffold is experimentally demonstrated, where the structure is annealed at 650°C for 2 hours in inert atmosphere [70]. The emission of this Mo-coated woodpile structure is measured at 620°C over the wavelength range 1.5 - 2.5 µm. Additionally, by annealing the structure at 650°C for 2 hours under inert atmosphere, the authors of Ref. [70] report that no grain growth of Mo is observed. A few more nanostructured emitters with Mo are reported based on simulation at wavelengths 1 - 4 µm [71]. Fabrication techniques of three-dimensional nanostructures with Mo are also reported for TPV applications [72]. Besides nanostructured emitters, an emitter based on optical interference between thin Mo and HfO_2 layers is demonstrated with measured emission at room temperature as well [73].

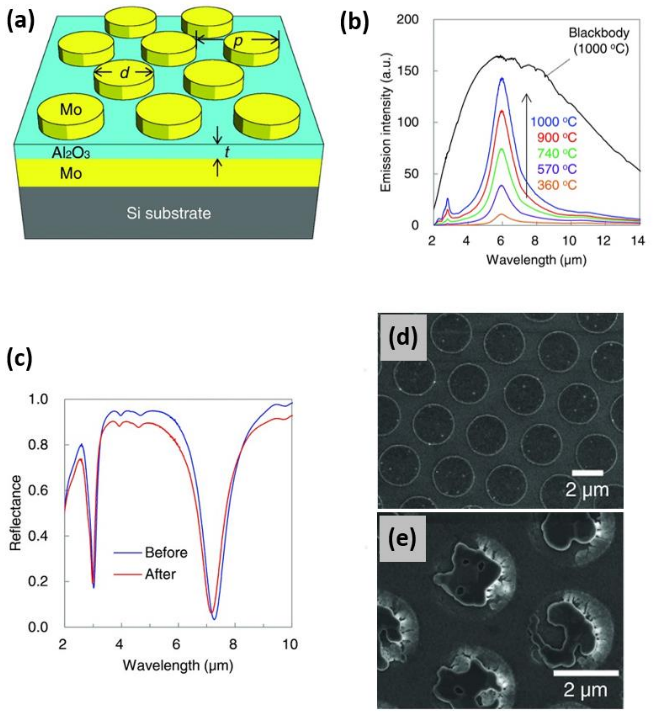

Fig. 14. A Mo-based emitter. Reprinted with permission from Ref. [69]. **(a):** Emitter structure. Thicknesses of the top and bottom Mo layers are 100 nm and 1 μm, respectively. **(b):** Measured emission of the emitter at several temperatures up to 1000°C in vacuum. **(c):** Measured reflectance of the emitter before and after annealing at 1000°C for 3 hours in vacuum. **(d)** and **(e)** are SEM images of undeformed and deformed Mo disks after annealing, respectively.

3.5. Ruthenium (Ru)

A Ru-based PhC absorber is experimentally demonstrated by Chou et al. [75]. The structure is also annealed at 1000°C for 24 hours in inert atmosphere. The results before and after annealing are shown in Fig. 15. The authors of Ref. [75] report mechanical deformation of the structure due to surface diffusion and delamination of Ru and HfO2. TiN is suggested as an adhesion layer, presumably between Ru and HfO2, to prevent delamination for their future work. Despite the deformation, the absorption results of the structure before and after annealing are reported to be similar.

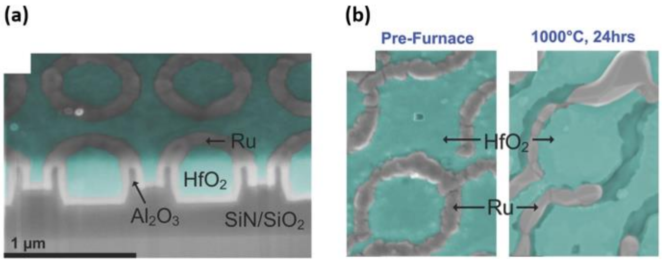

Fig. 15. A Ru-based photonic crystal. Reprinted with permission from Ref. [75]. **(a)**: A cross-section SEM image at an oblique angle. **(b)**: Top-view SEM images before (left) and after (right) annealing at 1000°C for 24 hours in inert atmosphere (95% Ar + 5% H_2).

3.6. Tantalum (Ta)

A nanostructured photonic crystal emitter made sorely out of Ta is experimentally reported by Rinnerbauer et al. [79]. The researchers of Ref. [79] etched a polycrystalline Ta wafer, 50.8 mm in diameter and 3 mm-thick, into a nanostructured emitter. Before patterning the structure, the Ta substrate was annealed at 2250°C for 4 hours in vacuum to induce grain growth for improved thermal stability at high temperatures. Grain sizes, after annealing, ranged from 0.1 – 0.5 mm and 1 – 2 mm. The research group of Ref. [79] further investigated thermal stability of their emitter with and without a 20 nm-thick HfO_2 coating layer by annealing the structure in vacuum in their other study [80]. The HfO_2, deposited on the emitter's surface, prevented surface diffusion of Ta and TaC formation – due to the C contamination in their vacuum chamber – on the Ta surface. Without the HfO_2 coating, the authors of Ref. [80] report that the structure's emission properties severely degrade due to the formation of TaC. The results before and after annealing the emitter with and without the HfO_2 coating are shown in Fig. 16. Besides, other nanostructured emitters fabricated with Ta are demonstrated based on simulation [81]. Fabrication techniques of three-dimensional nanostructures with Ta are reported for TPV applications as well [72].

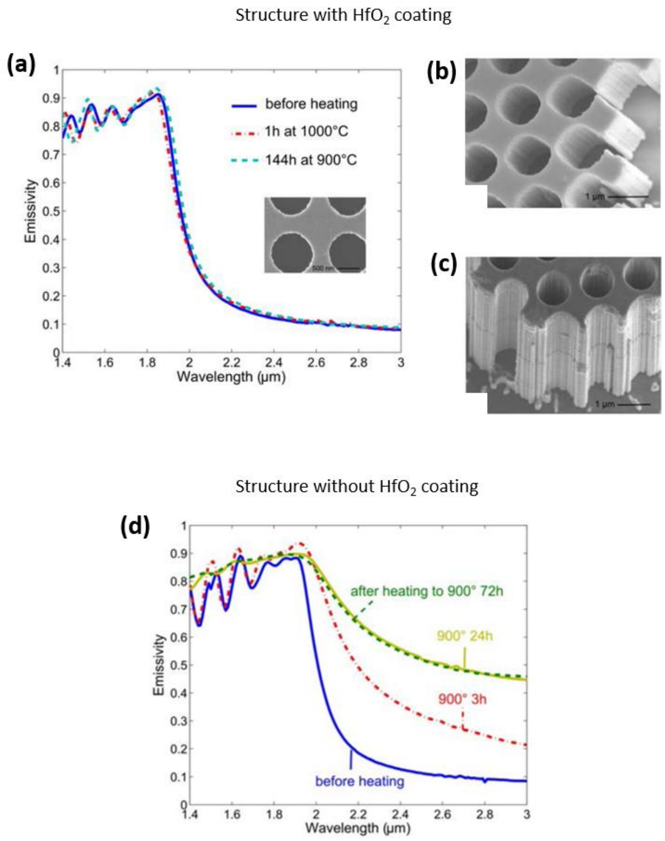

Fig. 16. Ta-based photonic crystal emitters with and without 20 nm-thick HfO_2 coating. Reprinted with permission from Ref. [80]. © The Optical Society. **(a):** Emissivity of the HfO_2-coated structure measured at room temperature before and after annealing in vacuum. **(b)** and **(c)** are SEM images of the HfO_2-coated structure (oblique view) before and after annealing at 900°C for 144h in vacuum, respectively. **(d):** Emissivity of the uncoated structure measured at room temperature before and after annealing in vacuum.

3.7. Tungsten (W)

Using a carbon nanotube (CNT) scaffold, Cui et al. experimentally demonstrated thermal stability of W-based photonic crystals [97]. W is deposited on an Al_2O_3-coated carbon nanotube scaffold. The results before and after annealing the structure at 1000°C in vacuum with He gas are shown in Fig. 17(a). In their X-ray diffraction (XRD) results, Fig. 17(a3), the slight shift and narrowing of the W (110) peak after annealing are due to the stress release and grain growth of nano-sized W grains. Meanwhile, Chang et al. conducted rigorous investigation of W-based metasurfaces with and without 20 nm-thick HfO_2 coating at 1200°C in vacuum [98]. HfO_2 is used to prevent evaporation of W. Fig. 17(b) shows absorption results of their HfO_2-coated metasurface before and after annealing in vacuum. The Ref. [98] also compares absorbance of their metasurfaces fabricated by two different deposition techniques for tungsten; sputtering and electron beam evaporation. Besides these structures, numerous emitters fabricated with W are demonstrated with their performance based on optical interference [39,46,99], complicated three-dimensional structures [70,72], and simulation [85–89,100] for high temperature applications. Nanostructured emitters made sorely out of bulk W are reported as well [49,90]. Moreover, there are a great deal of studies on W-based emitters for near-field TPV applications [65,91–94,96]. Near-field TPVs is distinguished from typical TPVs in that the spacing between the emitter and photodiode is on the nano or micrometer scale. One advantage of near-field TPVs is that the energy transfer from the emitter can exceed the theoretical blackbody limit [12,65]. One study experimentally shows that the TPV power output increases as the emitter-diode spacing decreases, where the emitter was in vacuum [65].

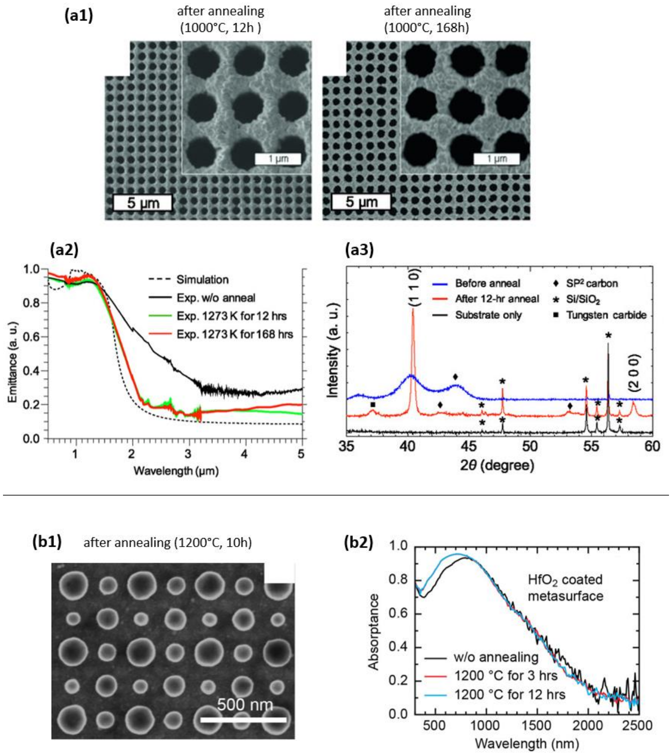

Fig. 17. W-based nanostructures for TPV emitters. **(a):** Results of the W-CNT structure (no surface coating of W) before and after annealing in vacuum [97]. SEM images (**a1**), measured emittance (**a2**), and XRD peaks (**a3**) are shown. The blue and red curves in the XRD results correspond to W. **(b):** Results of the 20 nm-thick HfO2-coated metasurface before and after annealing in vacuum [98]. An SEM image (**b1**) and measured absorptance (**b2**) are shown. **(a)** and **(b)** are reprinted with permission from Refs. [97] and [98], respectively.

3.8. Iridium (Ir)

A wafer-area emitter fabricated with Ir is experimentally demonstrated at room temperature in the visible to near-infrared spectrum by Oh et al. [103]. The absorption/emission of their emitter is due to optical interference effects. Ir is employed due to its higher resistance to oxidation. Fig. 18

shows the emitter structure and absorbance results in Ref. [103]. The research group of Ref. [103] also numerically proposes plasmonic MMs fabricated with Ir for emitter applications at wavelengths near 2 – 7 μm [104]. They show that the absorbance spectrum of their plasmonic MMs can be engineered by changing the width of the top features as the plasmonic resonance is responsible for its emission. Similar structures fabricated with Ir are reported based on simulation for longer wavelengths [105].

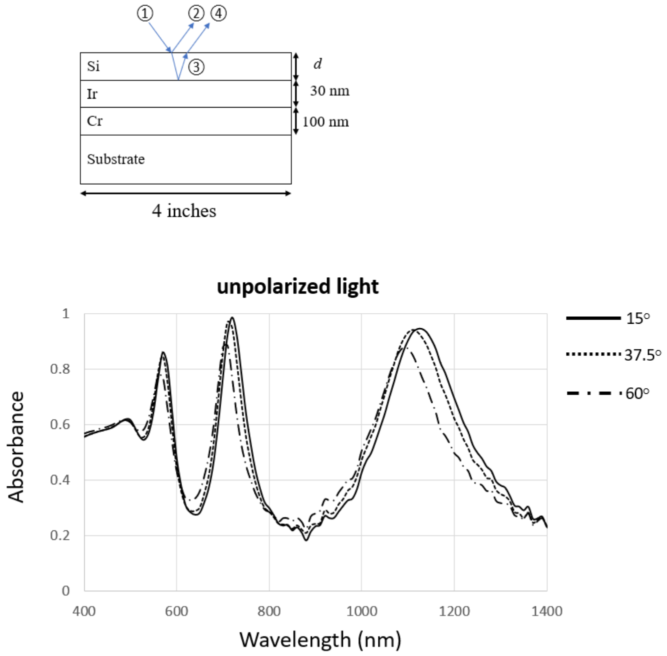

Fig. 18. An Ir-based emitter. Reprinted with permission from Ref. [103]. Absorbance results (for *d* = 225 nm) measured at room temperature are shown for unpolarized light. The incidence angles are denoted in the legend.

3.9. Platinum (Pt)

A Pt-based MM emitter with two-dimensional patterns is experimentally demonstrated at wavelengths near 600 – 1600 nm by Shemelya et al. [106]. The authors of Ref. [106] report optical properties of the emitter at high temperatures as well as before and after annealing. Fig. 19(a) shows their emitter structure and emissivity. Compared to two-dimensionally patterned MMs, three-dimensionally patterned MM emitters fabricated with Pt are demonstrated by Garín et al. at wavelengths near 2 – 10 μm [107]. The authors of Ref. [107] present optical and microstructure results of their emitters after annealing in air and N_2 atmosphere each. Fig. 19(b) shows these results. Effects of a dielectric coating layer on Pt-based MMs are also studied by other research groups [108,109]. By annealing at 1027°C for up to 12 minutes in Ar atmosphere, the authors of Ref. [108] show improved thermal stability of their Pt-based MMs with 150 nm-thick Al_2O_3 coating (Fig. 20). Other Pt-based emitters are experimentally demonstrated at relatively low temperatures [110,111].

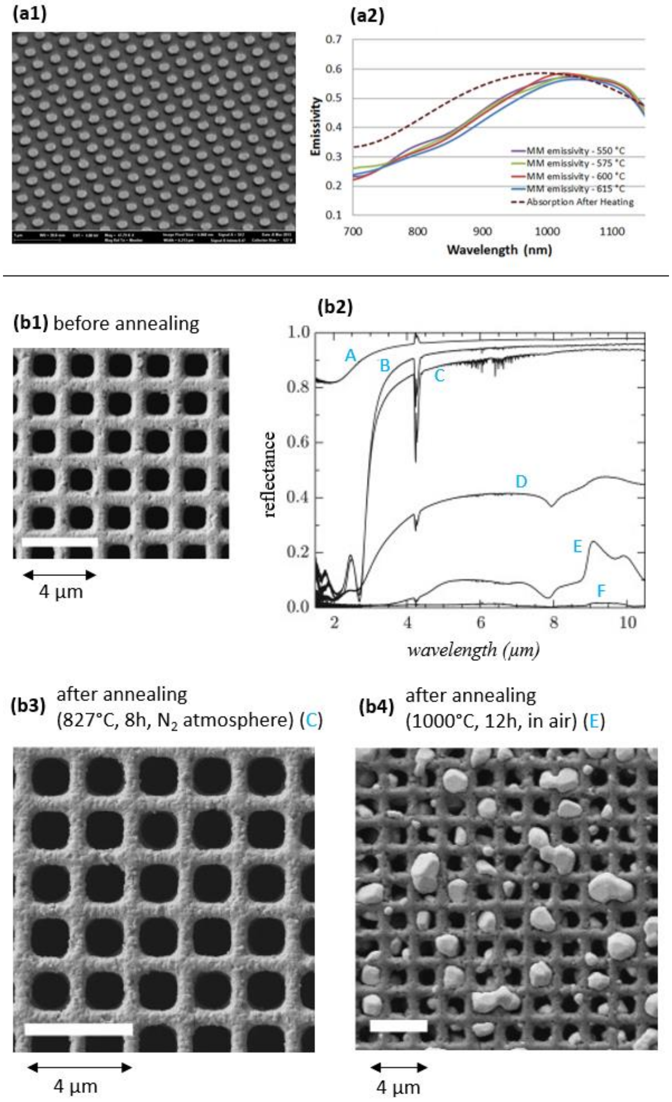

Fig. 19. Pt-based emitters (without surface coating). **(a):** Surface SEM image (**a1**) and measured emissivity (**a2**) of the two-dimensionally patterned metamaterial [106]. **(b):** Results of the three-dimensionally patterned metamaterial [107]. Surface SEM images before (**b1**) and after (**b3** and **b4**) annealing with corresponding measured reflectance (**b2**) are shown. Annealing conditions are written on top of each SEM image. **(a)** and **(b)** are reprinted with permission from Refs. [106] and [107], respectively.

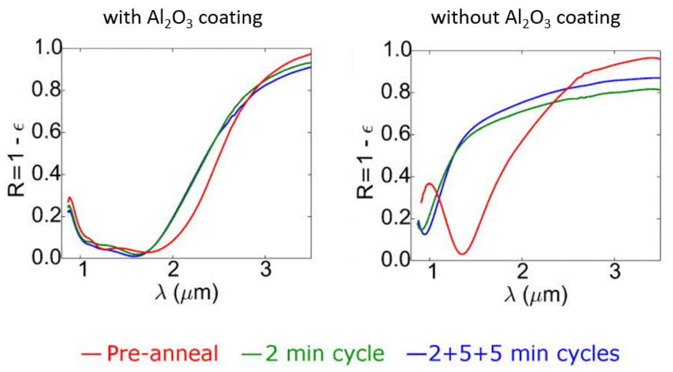

Fig. 20. Measured reflectance (R) of Pt-based MM emitters with and without 150 nm-thick Al_2O_3 coating after annealing at 1027°C in Ar atmosphere. The legend shows annealing time, where the font color corresponds to the plot color. ϵ is emissivity. Reprinted with permission from Ref. [108].

4. Discussion

4.1. Crystal structure

This work finds that most refractory emitters are fabricated with FCC or BCC metals. While these two crystal structures are optically isotropic, there remains a question as to how the anisotropic optical properties of HCP metals will affect the emitter's performance. As discussed in Sections 1.2 and 1.5, metals undergo grain growth at higher temperatures, and HCP metals become more anisotropic. We remind that TPV emitters typically remain at temperatures around 900K for their operation. For this reason, significant grain growth is expected to occur in emitter materials during their operation. In response to grain growth, the HCP metal's refractive index would change in preference of the dominant grains' crystallographic directions, as seen in Fig. 10. The refractive index variation is not desired since the emitter's optical performance is impacted by the materials' refractive index and it may lose its initially designed emission properties as a result of grain growth. Therefore, FCC or BCC metals may be preferable to HCP metals because the emission spectrum of TPV emitters should remain constant with time. However, for some HCP metals where the refractive index does not vary as much with crystalline direction, Ru for example [75], the above concern could be reduced.

4.2. Phase change

Zr and Hf undergo phase change from HCP into BCC at 863℃ and 2115°C, respectively. The BCC structure has a benefit of being optically isotropic. However, a phase transition involves abrupt changes in material properties such as lattice constants or volume. Since these changes can cause stress at the interface with a different material, it could lead to delamination and permanent fracture. For this reason, caution may be needed when using phase-changing materials in TPV emitters. However, if the TPV operation temperature is far below the phase transition temperature, the above concern could be reduced.

4.3. Oxidation

TPV emitters operate in a hot environment where their performance can degrade due to oxidation as well. For this reason, oxidation is probably one of the most important aspects to overcome for practical deployment of TPV technology in air. Several studies suggest that the oxidation rate of materials can vary due to stress in the oxide layer [123–125]. While these studies mainly focus on oxidation of bulk materials, the stress effect can be even more enlarged in oxidation of thin films since oxygen diffusion into the film is also affected by the compressive or tensile stress in the film. The stress in a thin film is dependent on numerous factors such as CTE or Young's modulus differences between the film and substrate, which are discussed in detail in Section 4.5, as well as deposition parameters [126] and thickness of the film. If an adhesion/buffer layer is used between the film and substrate, it shall also affect the stress in the film. Moreover, studies on metal oxidation report their results based on experimental parameters which vary largely from study to study; such as oxygen pressure, temperature, or annealing time [127–130], to which oxidation rate is sensitive. To the best of our knowledge, no study has yet been done where it compares oxidation characteristics of various refractory metal thin films with the same thickness on the same substrate for varying deposition parameters. For these reasons, it may be hard to directly compare oxidation characteristics of thin metal films, which are commonly used to fabricate selective TPV emitters. The standard reduction potential (SRP), however, as discussed in Section 1.4, are measured under consistent experimental parameters; 25℃, 1atm gas pressure, and solution concentration 1 mol/L [52]. For this reason, the SRPs could serve as a more objective measure to compare metal oxidation for TPV emitters.

4.4. Diffusion

Compared to diffusion through the volume of a material, surface diffusion depends on numerous factors such as geometry [47], surface energy [47], or surface contamination [131]. Surface contamination also impacts surface energy, which then affects surface diffusion rate [46]. By assuming no surface contamination, Ref. [47] shows surface diffusion rate of a PhC emitter as a function of surface geometry as well as emissivity degradation due to the mechanical structure change caused by diffusion. As the study finds, surface diffusion rate is proportional to diffusion coefficient of the material [47], which is discussed in Section 2 above. Since surface diffusion is dependent on numerous factors, a rigorous investigation of surface diffusion properties of emitters fabricated with various subwavelength patterns is expected to be highly time-consuming. Perhaps this explains the scarcity of the data. However, diffusion coefficient is one of the dominant parameters for surface diffusion and is independent of surface energy or contamination [47]. For this reason, diffusion coefficient could serve as a more objective measure to estimate mechanical stability of emitters against diffusion. In addition, as discussed in Section 3, refractory oxide coating layers contribute to reducing surface diffusion of metals. This can help emitters retain their initially designed structure.

4.5. Thermal expansion and stress

Different materials may have a different CTE. Stress at material interfaces due to different thermal expansion rates can cause delamination or destruction of the structure upon temperature changes. Therefore, researchers have taken CTE into account to minimize stress due to thermal expansion differences in their emitter. For example, if the CTE difference is too high, a material that has an in-between CTE is used as an adhesion (or buffer) layer [132]. In addition to CTE, stress-strain responses of the material, such as Young's modulus, may also be responsible for delamination as well. For example, we compare delamination results of Ti and Ir on a sapphire substrate. Although the sapphire's CTE is better matched to the Ir's than Ti's, it was reported that Ti improves adhesion between a sapphire substrate and an Ir layer, which delaminated off the sapphire without Ti [50]. The CTEs and Young's moduli of these materials are shown in Table 2. As it can be seen in the table, the Young's modulus of Ir is more than four times larger than that of Ti. This, despite the better CTE match with the sapphire's, might have created more stress at the Ir/sapphire interface. To map the relative stress in these layers at an increased temperature, we performed simulation. Fig. 21 shows the simulated relative stress for Ir, Ti, and Ir/Ti layers on a sapphire substrate at 100°C. In the figure, the Ir/sapphire structure is under a higher stress, Fig. 21(a), than the Ti/sapphire is, Fig. 21(b). These results may be interpreted that the higher Young's modulus of Ir is responsible for the observed delamination in Ref. [50]. Moreover, interestingly, more stress is present at the Ir/Ti interface, Fig. 21(c) than that at the Ir/sapphire interface, Fig. 21(a). However, as discussed above, Ir/Ti on a sapphire did not delaminate while Ir on a sapphire delaminated. This may be attributed to the fact that both Ir and Ti are metals and therefore, they bond stronger via metallic bonding than Ir (metallic bonding) and sapphire (ionic bonding) does. While many of failure issues arise at interfaces, some emitters are made sorely of one material with micro/nano patterns directly etched into the metal substrate [49,79,80,90] -referred to as "single-material emitter" hereafter. These emitters may exhibit advantages of no delamination compared to emitters that have interfaces.

Table 2. Coefficient of linear thermal expansion (CTE) and Young's modulus of Ti [53], Ir, and sapphire [113]. Given values are for polycrystals at room temperature.

	Ti	**Ir**	**Sapphire**
CTE (10^{-6}/K)	8.35	6.8	5.5
Young's modulus (GPa)	120	528	400

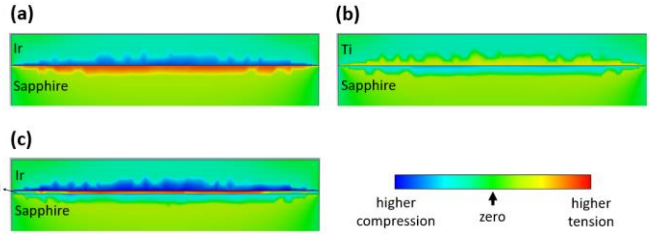

Fig. 21. Simulated relative stress in layers at 100°C. Thickness ratio of the layers used in simulation is Ir : sapphire = 1 : 10 (**a**), Ti : sapphire = 1 : 10 (**b**), and Ir : Ti : sapphire = 1 : 0.1 : 10 (**c**). Note that the results screenshots are cut at the sapphire. Layers are assumed to have been deposited at room temperature. Material properties at room temperature are used for simplified simulation.

4.6. Material cost

While the physical and chemical properties of materials determine the emitter's performance, enabling TPV applications on a larger scale may require lower material cost [133]. Assuming only metal prices in an emitter, metals with a lower price such as Nb, Mo, or Ta for example, as shown in Fig. 9(g), seem the best candidates to manufacture TPV emitters with for a lower cost. However, as the amount of materials used also impacts the cost, emitter design plays an important role in determining it as well. For example, Table 3 and Fig. 22 compare prices of several emitters on the actual amount of metal used. The emitter price (P) is calculated by the relationship $P = P_o \cdot A \cdot t \cdot \rho$, where P_o is metal price per unit weight, A is emitter surface area, t is emitter thickness, and ρ is metal density. The emitter price assumes only the price of the metal used. It is evident that single-material emitters tend to have much higher prices compared to metamaterial (MM) emitters due to the larger amount of material used. Thus, although single-material emitters have advantages of no delamination, as discussed in Section 4.5, they may require higher material cost. On the contrary, MM emitters can achieve much lower material cost although they may be more prone to delamination. Furthermore, we compare Rh (180 USD/g) and Mo (0.16 USD/g); the most expensive and cheapest metals amongst the 15 refractory metals in this study, respectively. Rh is 1125 times more expensive than Mo per unit weight. However, the price comparison in Table 3 suggests that Rh-based MM emitters can be even cheaper than Mo-based single-material emitters. Thus, we conclude that metal price should not be the only factor to look at when determining material cost but rather, both emitter design and metal price should be considered since the total cost of material is more important than the cost per weight.

Table 3. Price comparison of refractory metal-based emitters. Density data are from Ref. [52]. The thicknesses 1 mm (for single-material emitters) and 100 nm (for metamaterial emitters) are chosen as they are typical thicknesses of metal substrates and metal thin films in a metamaterial, respectively. "MM" in Emitter type stands for metamaterial. Emitter price assumes only the prices of the used metals in the emitter.

Metal	Density (ρ) (g/cm^3)	Price per unit weight (P_o) (USD/g)	Emitter surface area (A) (cm^2)	Emitter thickness (t)	Emitter price (P) (USD)	Emitter type
V	6.0	3	100	100 nm	0.018	MM
Cr	7.15	1	100	100 nm	0.0072	MM
Zr	6.52	4	100	100 nm	0.026	MM
Nb	8.57	0.5	100	100 nm	0.0043	MM
Mo	10.2	0.16	100	1 mm	16.3	Single-material
Mo	10.2	0.16	100	100 nm	0.0016	MM
Tc	11	100	100	100 nm	1.1	MM
Ru	12.1	25	100	100 nm	0.30	MM
Rh	12.4	180	100	100 nm	2.2	MM
Hf	13.3	2	100	100 nm	0.027	MM
Ta	16.4	2	100	100 nm	0.033	MM
W	19.3	2.9	100	1 mm	560	Single-material
W	19.3	2.9	100	100 nm	0.056	MM
Re	20.8	16	100	100 nm	0.33	MM
Os	22.59	100	100	100 nm	2.26	MM
Ir	22.56	100	100	100 nm	2.26	MM
Pt	21.5	15	100	100 nm	0.32	MM

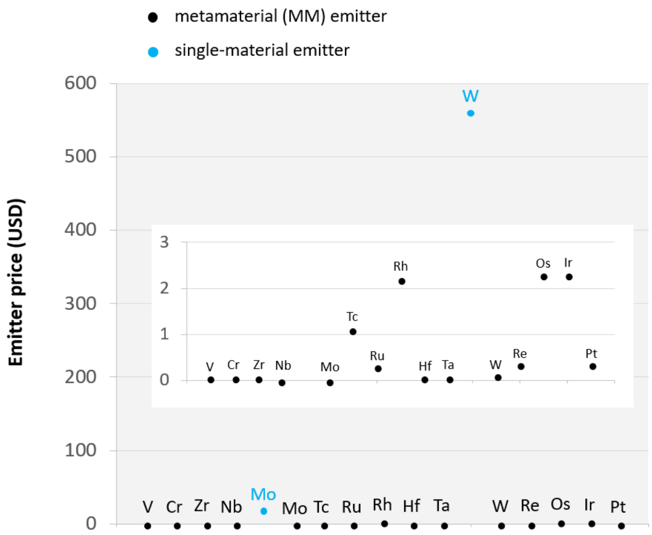

Fig. 22. Price comparison of emitters fabricated with refractory metals in Table 3. The constituent metal of the emitter is denoted by the element name on top of each data point.

5. Summary and Outlook

Selective TPV emitters fabricated with refractory metals are compared on their thermal stability. The emitter's performance can degrade due to a variety of reasons, such as mechanical deformation or chemical reaction. The material properties responsible for degradation of TPV emitters are reviewed: lattice constants, standard reduction potential (SRP), diffusion coefficient, Young's modulus (E_{Young}), and thermal expansion coefficient (CTE). These properties may serve as a measure to estimate thermal stability of emitters at higher temperatures. For example, a good material for TPV emitters may be the ones with the following properties: higher melting point, higher SRP, lower diffusion coefficient, lower E_{Young} as well as lower price. Lattice constants and CTE should also be matched between layers to minimize stress. Moreover, the material should not experience phase change at its operating temperature since it can lead to mechanical destruction. Larger grains are also preferred in the material to reduce diffusion, summarized in Fig. 23.

As shown in Table 1 and Fig. 9, all refractory metals in this review have both desired and undesired properties. This indicates that a specific property (or properties) may need to be more (or less) weighted when deciding the material. For example, for TPV applications in outer space [134,135], oxidation resistance may be less important. For applications in air, however, oxidation resistance shall be one of the most important criteria. This work finds that a dominant majority of TPV emitters in the literature are based on refractory metals that have poor oxidation resistance (SRP smaller than zero) and a relatively lower price. These emitters are also tested in vacuum or inert atmosphere. While they demonstrate their utility in non-oxidizing atmosphere, the thermal stability of these emitters may need to be tested in air for their applications in air. Many sites for potential deployment of TPV energy harvesting are industrial high-temperature processes [2–7] and power plants [8]. Since these sites are all under air, more research would also be needed on emitters fabricated with oxidation-resistant materials. Thus, refractory metals that have a positive, higher SRP such as Ru, Rh, or Ir could be a good candidate. These metals are costly compared to the metals above that are widely studied for TPV emitters. However, as discussed in Section 4.6, material cost can be reduced by using metamaterial emitters.

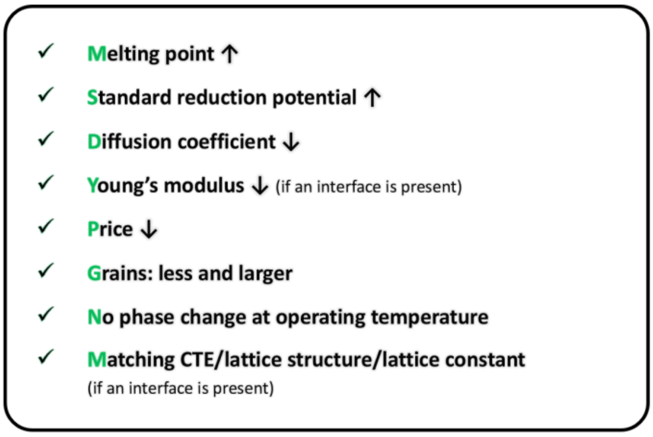
- ✓ **Melting point ↑**
- ✓ **Standard reduction potential ↑**
- ✓ **Diffusion coefficient ↓**
- ✓ **Young's modulus ↓** (if an interface is present)
- ✓ **Price ↓**
- ✓ **Grains: less and larger**
- ✓ **No phase change at operating temperature**
- ✓ **Matching CTE/lattice structure/lattice constant** (if an interface is present)

Fig. 23. Desired properties for a good material candidate for TPV emitters. Upward (↑) and downward (↓) arrows indicate higher and lower, respectively.

Acknowledgement

Funding was provided by the Office of Naval Research (ONR, Grant No. N00014-15-1-2946), Air Force Office of Scientific Research (AFOSR, Grant No. FA9550-20-1-0188), and National Science Foundation (NSF, Grant No. ECCS-1806311 and ECCS-2120568).

Conflicts of interest

There are no conflicts to declare

References

[1] Lawrence Livermore National Laboratory*, Estimated U.S. Energy Consumption, (https://flowcharts.llnl.gov).*

[2] T. Bauer, R. P. Forbes, and N. Pearsall, *The Potential of Thermophotovoltaic Heat Recovery for the Glass Industry*, *AIP Conference Proceedings*, Vol. 653 (AIP, 2003), pp. 101–110.

[3] T. Bauer, I. Forbes, and N. Pearsall, *The Potential of Thermophotovoltaic Heat Recovery for the UK Industry*, Int. J. Ambient Energy **25**, 19 (2004).

[4] L. M. Fraas, *Economic Potential for Thermophotovoltaic Electric Power Generation in the Steel Industry*, 2014 IEEE 40th Photovolt. Spec. Conf. PVSC 2014 766 (2014).

[5] E. Shoaei, *Performance Assessment of Thermophotovoltaic Application in Steel Industry*, Sol. Energy Mater. Sol. Cells **157**, 55 (2016).

[6] G. Bianchi, G. P. Panayiotou, L. Aresti, S. A. Kalogirou, G. A. Florides, K. Tsamos, S. A. Tassou, and P. Christodoulides, *Estimating the Waste Heat Recovery in the European Union Industry*, Energy, Ecol. Environ. **4**, 211 (2019).

[7] US Department of Energy, *Waste Heat Recovery: Technology and Opportunities in U.S. Industry*, 2008.

[8] W. E. S. W. A. Rashid, P. J. Ker, M. Z. Bin Jamaludin, M. M. A. Gamel, H. J. Lee, and N. B. A. Rahman, *Recent Development of Thermophotovoltaic System for Waste Heat Harvesting Application and Potential Implementation in Thermal Power Plant*, IEEE Access **8**, 105156 (2020).

[9] M. Suemitsu, T. Asano, T. Inoue, and S. Noda, *High-Efficiency Thermophotovoltaic System That Employs an Emitter Based on a Silicon Rod-Type Photonic Crystal*, ACS Photonics **7**, 80 (2020).

[10] D. N. Woolf, E. A. Kadlec, D. Bethke, A. D. Grine, J. J. Nogan, J. G. Cederberg, D. Bruce Burckel, T. S. Luk, E. A. Shaner, and J. M. Hensley, *High-Efficiency Thermophotovoltaic Energy Conversion Enabled by a Metamaterial Selective Emitter*, Optica **5**, 213 (2018).

[11] Y. X. Yeng, W. R. Chan, V. Rinnerbauer, J. D. Joannopoulos, M. Soljačić, and I. Celanovic, *Performance Analysis of Experimentally Viable Photonic Crystal Enhanced Thermophotovoltaic Systems*, Opt. Express **21**, A1035 (2013).

[12] A. Fiorino, L. Zhu, D. Thompson, R. Mittapally, P. Reddy, and E. Meyhofer, *Nanogap Near-Field Thermophotovoltaics*, Nat. Nanotechnol. **13**, 806 (2018).

[13] T. C. Narayan, L. Y. Kuritzky, D. P. Nizamian, B. A. Johnson, E J. Tervo, A. R. Young, C. Luciano, M. K. Arulanandam, B. M. Kayes, E. E. Perl et al.*, World Record Demonstration of > 30% Thermophotovoltaic Conversion Efficiency, 47th IEEE Photovoltaic Specialists Conference (PVSC) (IEEE, 2020), pp. 1792–1795.*

[14] N. A. Pfiester and T. E. Vandervelde, *Selective Emitters for Thermophotovoltaic Applications*, Phys. Status Solidi Appl. Mater. Sci. **214**, 1 (2017).

[15] M. Oh, E. Carlson, and T. E. Vandervelde, *Design of an All-Semiconductor Selective Metamaterial Emitter in the Mid-IR Regime with Larger Feature Sizes for Thermophotovoltaic Energy Conversion Applications*, J. Electron. Mater. (2020).

[16] A. Licht, N. Pfiester, D. DeMeo, J. Chivers, and T. E. Vandervelde, *A Review of Advances in Thermophotovoltaics for Power Generation and Waste Heat Harvesting*, MRS Adv. **4**, 2271 (2019).

[17] R. Sakakibara, V. Stelmakh, W. R. Chan, M. Ghebrebrhan, J. D. Joannopoulos, M. Soljačić, and I. Čelanović, *Practical Emitters for Thermophotovoltaics: A Review*, J. Photonics Energy **9**, 1 (2019).

[18] M. Oh and T. Vandervelde, *Bridging the Gaps between Different Sign Conventions of Fresnel Reflection Coefficients towards a Universal Form*, in *Midwest Symposium on*

Circuits and Systems, Vol. 2020August (2020), pp. 707–713.

[19] W. D. Hershberger, *The Absorption of Microwaves by Gases*, J. Appl. Phys. **17**, 495 (1946).

[20] W. D. Callister, *Materials Science and Engineering: An Introduction*, 7th ed. (John Wiley & Sons, Inc., 2007).

[21] A. Yariv and P. Yeh, *Optical Waves in Crystals: Propagation and Control of Laser Radiation.* (Wiley & Sons, Inc., 1984).

[22] J. B. WACHTMAN, T. G. SCUDERI, and G. W. CLEEK, *Linear Thermal Expansion of Aluminum Oxide and Thorium Oxide from 100 to 1100K*, J. Am. Ceram. Soc. **45**, 319 (1962).

[23] Y. J. Kim, J. U. Lee, Y. M. Kim, and S. H. Park, *Microstructural Evolution and Grain Growth Mechanism of Pre-Twinned Magnesium Alloy during Annealing*, J. Magnes. Alloy. (2020).

[24] V. Rinnerbauer, S. Ndao, Y. X. Yeng, W. R. Chan, J. J. Senkevich, J. D. Joannopoulos, M. Soljačić, and I. Celanovic, *Recent Developments in High-Temperature Photonic Crystals for Energy Conversion*, Energy Environ. Sci. **5**, 8815 (2012).

[25] I. Schnell and R. C. Albers, *Zirconium under Pressure: Phase Transitions and Thermodynamics*, J. Phys. Condens. Matter **18**, 1483 (2006).

[26] A. O'Hara and A. A. Demkov, *Oxygen and Nitrogen Diffusion in α-Hafnium from First Principles*, Appl. Phys. Lett. **104**, (2014).

[27] T. P. Leervad Pedersen, J. Kalb, W. K. Njoroge, D. Wamwangi, M. Wuttig, and F. Spaepen, *Mechanical Stresses upon Crystallization in Phase Change Materials*, Appl. Phys. Lett. **79**, 3597 (2001).

[28] B. Šavija, *Smart Crack Control in Concrete through Use of Phase Change Materials (PCMs): A Review*, Materials (Basel). **11**, (2018).

[29] V. Sanphuang, N. Ghalichechian, N. K. Nahar, and J. L. Volakis, *Reconfigurable THz Filters Using Phase-Change Material and Integrated Heater*, IEEE Trans. Terahertz Sci. Technol. **6**, 583 (2016).

[30] Z. Shao, X. Cao, H. Luo, and P. Jin, *Recent Progress in the Phase-Transition Mechanism and Modulation of Vanadium Dioxide Materials*, NPG Asia Mater. **10**, 581 (2018).

[31] C. Kittel, *Introduction to Solid State Physics*, 8th ed. (John Wiley and Sons, Inc., 2005).

[32] R. H. Petrucci, R. Petrucci, F. G. Herring, J. Madura, and C. Bissonnette, *General Chemistry: Principles and Modern Applications*, 11th ed. (Pearson, 2017).

[33] A. G. Milnes and D. Feucht, *Heterojunctions and Metal-Semiconductor Junctions* (Academic Press, 1972).

[34] R. M. Cannon, R. M. Fisher, and A. G. Evans, *Decohesion of Thin Films From Ceramic Substrates*, MRS Proc. **54**, 799 (1985).

[35] H. Yu and J. W. Hutchinson, *Delamination of Thin Film Strips*, Thin Solid Films **423**, 54 (2003).

[36] P. Flowers, K. Theopold, and R. Langley, *Standard Reduction Potentials*, (https://chem.libretexts.org/@go/page/210168).

[37] C. Schaller, *Reduction Potential*, (https://chem.libretexts.org/@go/page/190005).

[38] P. N. Dyachenko, S. Molesky, A. Y. Petrov, M. Störmer, T. Krekeler, S. Lang, M. Ritter, Z. Jacob, and M. Eich, *Controlling Thermal Emission with Refractory Epsilon-near-Zero Metamaterials via Topological Transitions*, Nat. Commun. **7**, (2016).

[39] M. Chirumamilla, A. S. Roberts, F. Ding, D. Wang, P. K. Kristensen, S. I. Bozhevolnyi, and K. Pedersen, *Multilayer Tungsten-Alumina-Based Broadband Light Absorbers for High-Temperature Applications*, Opt. Mater. Express **6**, 2704 (2016).

[40] Y. Zhang, K. Li, X. Yang, S. Cao, H. Pang, Q. Cai, Q. Ye, and X. Wu, *Thermal Degradation of Tungsten Nanowire-Based Hyperbolic Metamaterial Emitters for Near-Field Thermophotovoltaic Applications*, Int. J. Thermophys. **43**, 1 (2022).

[41] B. Striggow, *Field Measurement of Oxidation-Reduction Potential (ORP)*, 2017.

[42] D. C. Harris, *Quantitative Chemical Analysis* (W. H. Freeman & Company, 2016).

[43] A. H. Chokshi, *Diffusion, Diffusion Creep and Grain Growth Characteristics of Nanocrystalline and Fine-Grained Monoclinic, Tetragonal and Cubic Zirconia*, Scr. Mater. **48**, 791 (2003).

[44] H. Hernandez, *Standard Maxwell-Boltzmann Distribution: Definition and Properties*, ForsChem Res. Reports 16 (2017).

[45] J. H. Kim, S. M. Jung, and M. W. Shin, *Thermal Degradation of Refractory Layered Metamaterial for Thermophotovoltaic Emitter under High Vacuum Condition*, Opt. Express **27**, 3039 (2019).

[46] M. Chirumamilla, G. V. Krishnamurthy, K. Knopp, T. Krekeler, M. Graf, D. Jalas, M. Ritter, M. Störmer, A. Y. Petrov, and M. Eich, *Metamaterial Emitter for Thermophotovoltaics Stable up to 1400 °C*, Sci. Rep. **9**, 1 (2019).

[47] D. Peykov, Y. X. Yeng, I. Celanovic, J. D. Joannopoulos, and C. A. Schuh, *Effects of Surface Diffusion on High Temperature Selective Emitters*, Opt. Express **23**, 9979 (2015).

[48] T. Vasilos and J. T. Smith, *Diffusion Mechanism for Tungsten Sintering Kinetics*, J. Appl. Phys. **35**, 215 (1964).

[49] H. Sai, Y. Kanamori, and H. Yugami, *High-Temperature Resistive Surface Grating for Spectral Control of Thermal Radiation*, Appl. Phys. Lett. **82**, 1685 (2003).

[50] N. A. Pfiester, *Metamaterial Devices for Enhancement of Thermophotovoltaics and Mid-IR Detectors*, Tufts University, 2019.

[51] J. R. Davis, editor , *Metals Handbook Desk Edition*, 2nd ed. (ASM International, 1998).

[52] W. Haynes, D. Lide, and T. Bruno, *Handbook of Chemistry and Physics 97th Ed.* (CRC Press, 2016).

[53] F. Cardarelli, *Materials Handbook*, 3rd ed. (Springer International Publishing, Cham, 2018).

[54] T. Górecki, *The Relations between the Shear Modulus, the Bulk Modulus and Young's Modulus for Polycrystalline Metallic Elements*, Mater. Sci. Eng. **43**, 225 (1980).

[55] R. T. Downs and H.-W. Michelle, *The American Mineralogist Crystal Structure Database*, Am. Mineral. **88**, 247 (2003).

[56] R. F. Peart, *Diffusion of V48 and Fe59 in Vanadium*, J. Phys. Chem. Solids **26**, 1853 (1965).

[57] G. Neumann and C. Tuijn, *Self-Diffusion and Impurity*

Diffusion in Pure Metals: Handbook of Experimental Data (Elsevier, 2009).

[58] Y. S. Touloukian, *Thermal Expansion: Metallic Elements and Alloys (Thermophysical Properties of Matter, Vol. 12)* (IFI/Plenum, 1975).

[59] New Jersey Department of Health, *Workplace Health and Safety*, (https://web.doh.state.nj.us/rtkhsfs/factsheets.aspx).

[60] G. Liu, X. Liu, J. Chen, Y. Li, L. Shi, G. Fu, and Z. Liu, *Near-Unity, Full-Spectrum, Nanoscale Solar Absorbers and near-Perfect Blackbody Emitters*, Sol. Energy Mater. Sol. Cells **190**, 20 (2019).

[61] W. Gale and T. Totemeir, *Smithells Metals Reference Book*, 8th ed. (Elsevier, 2004).

[62] H. Deng, Z. Li, L. Stan, D. Rosenmann, D. Czaplewski, J. Gao, and X. Yang, *Broadband Perfect Absorber Based on One Ultrathin Layer of Refractory Metal*, Opt. Lett. **40**, 2592 (2015).

[63] D. Hu, H. Wang, Z. Tang, and X. Zhang, *Investigation of a Broadband Refractory Metal Metamaterial Absorber at Terahertz Frequencies*, Appl. Opt. **55**, 5257 (2016).

[64] Y. Li, Z. Liu, H. Zhang, P. Tang, B. Wu, and G. Liu, *Ultra-Broadband Perfect Absorber Utilizing Refractory Materials in Metal-Insulator Composite Multilayer Stacks*, Opt. Express **27**, 11809 (2019).

[65] G. R. Bhatt, B. Zhao, S. Roberts, I. Datta, A. Mohanty, T. Lin, J. M. Hartmann, R. St-Gelais, S. Fan, and M. Lipson, *Integrated Near-Field Thermo-Photovoltaics for Heat Recycling*, Nat. Commun. **11**, 1 (2020).

[66] A. Jain, S. Ping Ong, G. Hautier, W Chen, W. D. Richards, S. Dacek, S. Cholia, D. Gunter, D. Skinner, G. Ceder et al., *Commentary: The Materials Project: A Materials Genome Approach to Accelerating Materials Innovation*, APL Mater. **1**, (2013).

[67] S. Dierks, *Material Safety Data Sheet (Niobium)*.

[68] S. Bagheri, N. Strohfeldt, M. Ubl, A. Berrier, M. Merker, G. Richter, M. Siegel, and H. Giessen, *Niobium as Alternative Material for Refractory and Active Plasmonics*, ACS Photonics **5**, 3298 (2018).

[69] T. Yokoyama, T. D. Dao, K. Chen, S. Ishii, R. P. Sugavaneshwar, M. Kitajima, and T. Nagao, *Spectrally Selective Mid-Infrared Thermal Emission from Molybdenum Plasmonic Metamaterial Operated up to 1000 °C*, Adv. Opt. Mater. **4**, 1987 (2016).

[70] P. Nagpal, S. E. Han, A. Stein, and D. J. Norris, *Efficient Low-Temperature Thermophotovoltaic Emitters from Metallic Photonic Crystals*, Nano Lett. **8**, 3238 (2008).

[71] N. A. Pfiester, D. F. DeMeo, C. M. Shemela, and T. E. Vandervelde, *Thermophotovoltaic Efficiency Enhancement Through Metamaterial Selective Emitters*, 28th Eur. Photovolt. Sol. Energy Conf. Exhib, 2013, pp. 269–273.

[72] P. Nagpal, D. P. Josephson, N. R. Denny, J. Dewilde, D. J. Norris, and A. Stein, *Fabrication of Carbon/Refractory Metal Nanocomposites as Thermally Stable Metallic Photonic Crystals*, J. Mater. Chem. **21**, 10836 (2011).

[73] A. Kohiyama, M. Shimizu, and H. Yugami, *Unidirectional Radiative Heat Transfer with a Spectrally Selective Planar Absorber/Emitter for High-Efficiency Solar Thermophotovoltaic Systems*, Appl. Phys. Express **9**, (2016).

[74] N. Greenwood and A. Earnshaw, *Chemistry of the Elements*, 2nd ed. (Butterworth-Heinemann, 1998).

[75] J. B. Chou, Y. X. Yeng, Y. E. Lee, A. Lenert, V. Rinnerbauer, I. Celanovic, M. Soljačić, N. X. Fang, E. N. Wang, and S. G. Kim, *Enabling Ideal Selective Solar Absorption with 2D Metallic Dielectric Photonic Crystals*, Adv. Mater. **26**, 8041 (2014).

[76] S. Yadav and K. T. Ramesh, *The Mechanical Behavior of Polycrystalline Hafnium: Strain-Rate and Temperature Dependence*, Mater. Sci. Eng. A **246**, 265 (1998).

[77] Electronic Space Products International, *Material Safety Data Sheet (Hafnium), (https://www.espimetals.com/index.php/msds#H)*.

[78] Electronic Space Products International, *Material Safety Data Sheet (Tantalum), (https://www.espimetals.com/index.php/msds#H)*.

[79] V. Rinnerbauer, S. Ndao, Y. Xiang Yeng, J. J. Senkevich, K. F. Jensen, J. D. Joannopoulos, M. Soljačić, I. Celanovic, and R. D. Geil, *Large-Area Fabrication of High Aspect Ratio Tantalum Photonic Crystals for High-Temperature Selective Emitters*, J. Vac. Sci. Technol. B, Nanotechnol. Microelectron. Mater. Process. Meas. Phenom. **31**, 011802 (2013).

[80] V. Rinnerbauer, Y. X. Yeng, W. R. Chan, J. J. Senkevich, J. D. Joannopoulos, M. Soljačić, and I. Celanovic, *High-Temperature Stability and Selective Thermal Emission of Polycrystalline Tantalum Photonic Crystals*, Opt. Express **21**, 11482 (2013).

[81] W. Gu, G. Tang, and W. Tao, *High Efficiency Thermophotovoltaic Emitter by Metamaterial-Based Nano-Pyramid Array*, Opt. Express **23**, 30681 (2015).

[82] G. M. Neumann and W. Hirschwald, *Selbstdiffusion Und Diffusionsmechanismus in Wolfram*, Zeitschrift Fur Naturforsch. - Sect. A J. Phys. Sci. **21**, 812 (1966).

[83] S. L. Robinson and O. D. Sherby, *Mechanical Behavior of Polycrystalline Tungsten at Elevated Temperature*, Acta Metall. **17**, 109 (1969).

[84] G. B. Van Der Voet, T. I. Todorov, J. A. Centeno, W. Jonas, J. Ives, and F. G. Mullick, *Metals and Health: A Clinical Toxicological Perspective on Tungsten and Review of the Literature*, Mil. Med. **172**, 1002 (2007).

[85] J. Song, M. Si, Q. Cheng, and Z. Luo, *Two-Dimensional Trilayer Grating with a Metal/Insulator/Metal Structure as a Thermophotovoltaic Emitter*, Appl. Opt. **55**, 1284 (2016).

[86] A. Ghanekar, L. Lin, and Y. Zheng, *Novel and Efficient Mie-Metamaterial Thermal Emitter for Thermophotovoltaic Systems*, Opt. Express **24**, A868 (2016).

[87] F. T. Maremi, N. Lee, G. Choi, T. Kim, and H. H. Cho, *Design of Multilayer Ring Emitter Based on Metamaterial for Thermophotovoltaic Applications*, Energies **11**, 1 (2018).

[88] Y. B. Chen and Z. M. Zhang, *Design of Tungsten Complex Gratings for Thermophotovoltaic Radiators*, Opt. Commun. **269**, 411 (2007).

[89] G. Silva-Oelker, C. Jerez-Hanckes, and P. Fay, *High-Temperature Tungsten-Hafnia Optimized Selective Thermal Emitters for Thermophotovoltaic Applications*, J. Quant.

Spectrosc. Radiat. Transf. **231**, 61 (2019).

[90] I. Celanovic, N. Jovanovic, and J. Kassakian, *Two-Dimensional Tungsten Photonic Crystals as Selective Thermal Emitters*, Appl. Phys. Lett. **92**, (2008).

[91] N. Vongsoasup, M. Francoeur, and K. Hanamura, *Performance Analysis of Near-Field Thermophotovoltaic System with 2D Grating Tungsten Radiator*, Int. J. Heat Mass Transf. **115**, 326 (2017).

[92] J. Y. Chang, Y. Yang, and L. Wang, *Tungsten Nanowire Based Hyperbolic Metamaterial Emitters for Near-Field Thermophotovoltaic Applications*, Int. J. Heat Mass Transf. **87**, 237 (2015).

[93] T. Inoue, K. Watanabe, T. Asano, and S. Noda, *Near-Field Thermophotovoltaic Energy Conversion Using an Intermediate Transparent Substrate*, Opt. Express **26**, A192 (2018).

[94] J. K. Tong, W. C. Hsu, Y. Huang, S. V. Boriskina, and G. Chen, *Thin-Film "thermal Well" Emitters and Absorbers for High-Efficiency Thermophotovoltaics*, Sci. Rep. **5**, 1 (2015).

[95] M. Chirumamilla, G. V. Krishnamurthy, S. S. Rout, M. Ritter, M. Störmer, A. Y. Petrov, and M. Eich, *Thermal Stability of Tungsten Based Metamaterial Emitter under Medium Vacuum and Inert Gas Conditions*, Sci. Rep. **10**, 2 (2020).

[96] A. Datas and R. Vaillon, *Thermionic-Enhanced near-Field Thermophotovoltaics*, Nano Energy **61**, 10 (2019).

[97] K. Cui, P. Lemaire, H. Zhao, T. Savas, G. Parsons, and A. J. Hart, *Tungsten–Carbon Nanotube Composite Photonic Crystals as Thermally Stable Spectral-Selective Absorbers and Emitters for Thermophotovoltaics*, Adv. Energy Mater. **8**, 1 (2018).

[98] C.-C. Chang, W. J. M. Kort-Kamp, J. Nogan, T. S. Luk, A. K. Azad, A. J. Taylor, D. A. R. Dalvit, M. Sykora, and H.-T. Chen, *High-Temperature Refractory Metasurfaces for Solar Thermophotovoltaic Energy Harvesting*, Nano Lett. **18**, 7665 (2018).

[99] N. Jeon, J. J. Hernandez, D. Rosenmann, S. K. Gray, A. B. F. Martinson, and J. J. Foley IV, *Pareto Optimal Spectrally Selective Emitters for Thermophotovoltaics via Weak Absorber Critical Coupling*, Adv. Energy Mater. **8**, 1 (2018).

[100] A. Ghanekar, M. Sun, Z. Zhang, and Y. Zheng, *Optimal Design of Wavelength Selective Thermal Emitter for Thermophotovoltaic Applications*, J. Therm. Sci. Eng. Appl. **10**, 011004 (2018).

[101] I. C. Smith, B. L. Carson, and T. L, *Osmium : An Appraisal of Environ- Mental Exposure*, Environ. Heal. **8**, 201 (2000).

[102] G. F. Nordberg, B. A. Fowler, and M. Nordberg, *Handbook on the Toxicology of Metals: Fourth Edition* (Elsevier, 2014).

[103] M. Oh and T. E. Vandervelde, *Wafer-Area Selective Emitters Based on Optical Interference*, MRS Adv. (2021).

[104] M. Oh, E. S. Carlson, and T. E. Vandervelde, *Coupled Resonance via Localized Surface Plasmon Polaritons in Iridium-Based Refractory Metamaterials*, Comput. Mater. Sci. **197**, 110598 (2021).

[105] M. Oh, E. S. Carlson, and T. E. Vandervelde, *Localized Surface Plasmon Resonance in Refractory Metamaterials*, in *Advanced Fabrication Technologies for Micro/Nano Optics and Photonics XIV*, Vol. 11696 (SPIE, 2021), p. 40.

[106] C. Shemelya, D. Demeo, N. P. Latham, X. Wu, C. Bingham, W. Padilla, and T. E. Vandervelde, *Stable High Temperature Metamaterial Emitters for Thermophotovoltaic Applications*, Appl. Phys. Lett. **104**, (2014).

[107] M. Garín, D. Hernández, T. Trifonov, and R. Alcubilla, *Three-Dimensional Metallo-Dielectric Selective Thermal Emitters with High-Temperature Stability for Thermophotovoltaic Applications*, Sol. Energy Mater. Sol. Cells **134**, 22 (2015).

[108] D. Woolf, J. Hensley, J. G. Cederberg, D. T. Bethke, A. D. Grine, and E. A. Shaner, *Heterogeneous Metasurface for High Temperature Selective Emission*, Appl. Phys. Lett. **105**, 1 (2014).

[109] N. Pfiester, N. Naka, and T. Vandervelde, *Platinum Metamaterials For Thermophotovoltaic Selective Emitters*, *31st European Photovoltaic Solar Energy Conference and Exhibition* (2015), pp. 55–58.

[110] D. F. DeMeo, N. A. Pfeister, C. M. Shemelya, and T. Vandervelde, *Metamaterial Selective Emitters for Photodiodes*, in *Optical Components and Materials XI*, Vol. 8982 (2014), p. 89820J.

[111] M. Shimizu and H. Yugami, *Thermal Radiation Control by Surface Gratings as an Advanced Cooling System for Electronic Devices*, J. Therm. Sci. Technol. **6**, 297 (2011).

[112] R. E. Hann, P. R. Suitch, and J. L. Pentecost, *Monoclinic Crystal Structures of ZrO2 and HfO2 Refined from X-Ray Powder Diffraction Data*, J. Am. Ceram. Soc. **68**, C (1985).

[113] M. A. Aswad, *Residual Stress and Fracture in High Temperature Ceramics*, The University of Manchester, 2012.

[114] M. A. Hopcroft, W. D. Nix, and T. W. Kenny, *What Is the Young's Modulus of Silicon?*, J. Microelectromechanical Syst. **19**, 229 (2010).

[115] H.-J. Choi and Y. Kim, *Elastic Modulus of HfO2 Thin Film Grown by Atomic Layer Deposition with Wrinkle-Based Measurement*, Bull. Korean Chem. Soc. **38**, 1246 (2017).

[116] N. SOGA and O. L. ANDERSON, *High-Temperature Elastic Properties of Polycrystalline MgO and Al2O3*, J. Am. Ceram. Soc. **49**, 355 (1966).

[117] S. R. Skaggs, *Zero and Low Coefficient of Thermal Expansion Polycrystalline Oxides*, Los Alamos Scientific Lab., N.Mex. (USA), 1977.

[118] G. K. White and M. L. Minges, *Thermophysical Properties of Some Key Solids: An Update*, Int. J. Thermophys. **18**, 1269 (1997).

[119] M. Querry, *Optical Constants of Minerals and Other Materials from the Millimeter to the Ultraviolet*, US Army Armament, Munitions , 1987.

[120] E. D. Palik, *Handbook of Optical Constants of Solids (Vol. 3)* (Academic Press, 1998).

[121] A. LaPotin, K. L. Schulte, M. A. Steiner, K. Buznitsky, C. C. Kelsall, D. J. Friedman, E. J. Tervo, R. M. France, M. R. Young, A. Rohskopf et al., *Thermophotovoltaic Efficiency of 40%*, Nature **604**, 287 (2022).

[122] T. Inoue, M. De Zoysa, T. Asano, and S. Noda, *Realization of Narrowband Thermal Emission with Optical Nanostructures*, Optica **2**, 27 (2015).

[123] A. Fargeix and G. Ghibaudo, *Dry Oxidation of Silicon: A New Model of Growth Including Relaxation of Stress by Viscous*

Flow, J. Appl. Phys. **54**, 7153 (1983).

[124] S. A. Ajuria, P. U. Kenkare, A. Nghiem, and T. C. Mele, *Kinetic Analysis of Silicon Oxidations in the Thin Regime by Incremental Growth*, J. Appl. Phys. **76**, 4618 (1994).

[125] R. B. Marcus and T. T. Sheng, *The Oxidation of Shaped Silicon Surfaces*, J. Electrochem. Soc. **129**, 1278 (1982).

[126] D. M. Broadway, J. Weimer, D. Gurgew, T. Lis, B. D. Ramsey, S. L. O'Dell, M. Gubarev, A. Ames, and R. Bruni, *Achieving Zero Stress in Iridium, Chromium, and Nickel Thin Films*, EUV X-Ray Opt. Synerg. between Lab. Sp. IV **9510**, 95100E (2015).

[127] C. A. Krier and R. I. Jaffee, *Oxidation of the Platinum-Group Metals*, J. Less Common Met. **5**, 411 (1963).

[128] S. Kohli, D. Niles, C. D. Rithner, and P. K. Dorhout, *Structural and Optical Properties of Iridium Films Annealed in Air*, Adv. X-Ray Anal. **45**, 352 (2002).

[129] E. A. Gulbransen and K. F. Andrew, *Kinetics of the Oxidation of Pure Tungsten from 500° to 1300°C*, J. Electrochem. Soc. **107**, 619 (1960).

[130] S. A. Humphry-Baker and W. E. Lee, *Tungsten Carbide Is More Oxidation Resistant than Tungsten When Processed to Full Density*, Scr. Mater. **116**, 67 (2016).

[131] M. Pichaud and M. Drechsler, *A Field Emission Measurement of the Influence of Adsorption on Surface Self-Diffusion*, Surf. Sci. **32**, 341 (1972).

[132] L. Yan and J. A. Woollam, *Optical Constants and Roughness Study of Dc Magnetron Sputtered Iridium Films*, J. Appl. Phys. **92**, 4386 (2002).

[133] E. L. Ralph and M. C. FitzGerald, *Systems/Marketing Challenges for TPV*, AIP Conference Proceedings, Vol. 321 (AIP, 1995), pp. 315–321.

[134] V. L. Teofilo, P. Choong, J. Chang, Y. L. Tseng, and S. Ermer, *Thermophotovoltaic Energy Conversion for Space*, J. Phys. Chem. C **112**, 7841 (2008).

[135] F. A. Vicente, C. E. Kelly, and S. Loughin, *Thermophotovoltaic (TPV) Applications to Space Power Generation*, Proc. Intersoc. Energy Convers. Eng. Conf. **1**, 635 (1996).